

Rochester Institute of Technology

RIT Digital Institutional Repository

Theses

5-15-2023

Vibration Powder Dispensing and Gravity-Fed Powder Delivery for Directed Energy Deposition Additive Manufacturing Systems

Andrew Greeley
amg2335@rit.edu

Follow this and additional works at: <https://repository.rit.edu/theses>

Recommended Citation

Greeley, Andrew, "Vibration Powder Dispensing and Gravity-Fed Powder Delivery for Directed Energy Deposition Additive Manufacturing Systems" (2023). Thesis. Rochester Institute of Technology. Accessed from

This Dissertation is brought to you for free and open access by the RIT Libraries. For more information, please contact repository@rit.edu.

Vibration Powder Dispensing and Gravity-Fed Powder Delivery for Directed Energy Deposition Additive Manufacturing Systems

Andrew Greeley

Advisor: Dr. Denis Cormier

May 15th 2023

A dissertation submitted in partial fulfillment of the requirements for the degree of

Doctor of Philosophy in Mechanical and Industrial Engineering

Mechanical and Industrial Engineering PhD Program

Kate Gleason College of Engineering

Rochester Institute of Technology

Committee Approval:

Dr. Denis Cormier, Thesis Advisor Date

Dr. Iris Rivero, Committee Member Date

Dr. Satish Kandlikar, Committee Member Date

Dr. Robert Stevens, Committee Member Date

Dr. Christopher Lewis, Defense Chairperson Date

Dr. Katie McConky, Department Head Date

Table of Contents

- 1. Abstract 1
- 2. Introduction 2
 - 2.1. Directed Energy Deposition Background 2
 - 2.2. Applications 3
 - 2.2.1. High-performance Parts 3
 - 2.2.2. Repair and Remanufacture 4
 - 2.2.3. Multi-material Parts 4
 - 2.3. Conventional Powder Delivery Background 4
 - 2.4. Issue 1: Powder Capture Efficiency and Cost 5
 - 2.5. Issue 2: Composition Control and Multi-Material Parts 6
 - 2.6. Issue 3: Powder Delivery Control Lag 6
 - 2.7. Proposed System Design 7
 - 2.7.1. Vibration Powder Dispensing 7
 - 2.7.2. Gravity-Fed Powder Delivery 7
 - 2.8. Research Questions 9
 - 2.8.1. Question 1: Vibration Powder Dispensing Mass Flow Rate 9
 - 2.8.2. Question 2: Gravity-Fed Powder Delivery Capture Efficiency 9
 - 2.8.3. Question 3: Control Lag 9
- 3. Background and Literature Review 10
 - 3.1. DED Process 10
 - 3.2. Conventional Gas Stream Powder Delivery 10
 - 3.3. Vibration Powder Dispensing 11
 - 3.4. Models of Vibration Powder Dispensing 15
 - 3.5. Previous Work with Proposed Approach 15
- 4. Modeling Background: Contact Mechanics and the Discrete Element Method (DEM) 16
 - 4.1. Calculations in DEM 16
 - 4.2. Powder in DEM 16
 - 4.2.1. Powder Size and Shape Measurement 17
 - 4.3. Forces and Contact Models in DEM 20
 - 4.3.1. Particle-Particle Contacts Using the EEPA Model 20
 - 4.3.2. Material Properties in the EEPA Contact Model 23
 - 4.3.3. Particle-Equipment Contacts using the Hertz-Mindlin with JKR Adhesion Model 24
 - 4.3.4. Material Properties in the Hertz-Mindlin with JKR Adhesion Contact Model 25
 - 4.4. Calibrating a Material in DEM 25

4.4.1. Initial Properties	25
4.4.2. Particle Bulk Density	26
4.4.3. Tapped Density and Particle-Particle Coefficient of Static Friction	27
4.4.4. Static Angle of Repose and Particle-Particle Coefficient of Rolling Friction	28
4.4.5. Surface Adhesion and VPD Particle-Equipment Surface Energy	29
4.4.6. Particle-Particle Surface Energy	30
4.4.7. Final DEM Contact Model Properties	31
5. Vibration Powder Dispensing Mass Flow Rate	33
5.1. Experimental Setup	33
5.2. Simulation Setup	34
5.3. Results and Discussion	34
5.3.1. Initial Experiment	34
5.3.2. Screening Experiment	35
5.3.3. Detailed Experiment	35
5.3.4. Simulation Results	37
5.3.5. Additional Work with Powder Flow Variability	40
6. Gravity-Fed Powder Delivery Stream	42
6.1. Experimental Setup	42
6.2. Simulation Setup	44
6.3. Results and Discussion	45
6.3.1. Experimental Results	45
6.3.2. Simulation Results	47
6.3.3. Discussion	53
7. Control Lag	55
7.1. Experimental Setup	55
7.2. Results and Discussion	55
8. Powder Capture Efficiency	57
8.1. Experimental Setup	57
8.1.1. Equipment	57
8.1.2. Shielding Gas	59
8.1.3. Procedure	59
8.2. Results	59
9. Conclusions	63
9.1. Extensions and Future Work	64
10. References	65

List of Figures

Figure 1: Directed Energy Deposition Process Diagram.....	2
Figure 2: RIT Hybrid DED System.....	3
Figure 3: Conventional Powder Delivery System.....	5
Figure 4: Vibration Powder Dispensing Cross Section View.....	7
Figure 5: Gravity-Fed Powder Delivery Cross Section View.....	8
Figure 6: SEM Image of Powder Particles.....	17
Figure 7: Processed Image of Powder Particles.....	18
Figure 8: DEM Particle Shapes a) spherical b) oblong.....	19
Figure 9: Contact Model Schematic.....	20
Figure 10: Bulk Density Calibration Simulation.....	27
Figure 11: Tapped Density Calibration Simulation.....	28
Figure 12: Static Angle of Repose Calibration Simulation.....	29
Figure 13: Equipment Adhesion Calibration Simulation.....	30
Figure 14: Experimental VPD Setup.....	33
Figure 15: VPD Simulation Setup.....	34
Figure 16: Main Effects for Screening VPD Experiment.....	35
Figure 17: Detailed VPD Experimental Results.....	36
Figure 18: Simulation and Experimental VPD Result Comparison.....	37
Figure 19: VPD Simulation Incline Comparison (Diameter=1038 μm).....	39
Figure 20: Hall Flow of Powder at Different Humidity Levels.....	41
Figure 21: GPD Experimental Setup.....	43
Figure 22: GPD Simulation Setup.....	45
Figure 23: Main Effects for GPD Experimental Spread.....	46
Figure 24: Main Effects for GPD Experimental Exit Velocity.....	47
Figure 25: Main Effects Plot for Spread in GPD Simulations.....	48
Figure 26: GPD Simulation Spread Main Effects Plots Divided.....	49
Figure 27: GPD Simulation Spread Interaction Plot.....	50
Figure 28: Main Effects Plot for Velocity in GPD Simulations.....	51
Figure 29: GPD Simulation Velocity Main Effects Plots Divided.....	52
Figure 30: GPD Simulation Velocity Interaction Plot.....	53
Figure 31: Velocity and Spread Correlation for All Conditions.....	54
Figure 32: Velocity and Spread for Subsets of Conditions.....	54
Figure 33: Control Lag Comparison.....	56
Figure 34: Powder Capture Efficiency Experimental System: a) system components, b) system after printing, c) system during printing.....	58
Figure 35: Comparison of Printed Tracks from Experimental and Conventional Systems in As Printed and Cleaned Conditions.....	62

List of Tables

Table 1: Operating Costs for Titanium Parts with 50% Powder Capture Efficiency	6
Table 2: Operating Costs for Stainless Steel Parts with 100% Powder Capture Efficiency	6
Table 3: Summary of Powder Capture Efficiencies.....	11
Table 4: Summary of Vibration Powder Dispensing Literature.....	13
Table 5: Measured Particle Size Distributions.....	19
Table 6: Initial Properties for Particle-Particle Contact Model.....	26
Table 7: Initial Properties for Particle-Equipment Contact Model.....	26
Table 8: Factors and Levels for Static Angle of Repose Calibration Simulations	29
Table 9: Factors and Levels for VPD Particle-Equipment Surface Energy Calibration Simulations	30
Table 10: Particle-Particle Surface Energy Calibration Data	31
Table 11: Final Particle-Particle Contact Model Properties	31
Table 12: Final Particle-Equipment Contact Model Properties	32
Table 13: Factors and Levels for Screening VPD Experiment	35
Table 14: Factors and Levels for Detailed VPD Experiment	36
Table 15: GPD Experiment Factors and Levels	44
Table 16: GPD Simulation Factors and Levels	45
Table 17: Powder Capture Efficiency Experiment Conditions	60
Table 18: Experimental Powder Capture Efficiency Results.....	60
Table 19: Conventional System Powder Capture Efficiency Test Settings	61

1. Abstract

Directed energy deposition is a class of additive manufacturing processes where focused thermal energy melts and fuses material being deposited on a part. This type of process is useful for making high performance parts, remanufacturing and repair, and for making multi-material parts. However, in systems where powder feedstock is used, only a fraction of the powder ends up in the part and the rest is usually wasted. Increasing the amount of powder captured in powder-fed directed energy deposition systems is the focus of this work.

The proposed solution is to combine vibration powder dispensing and gravity-fed powder delivery systems to give very high levels of powder capture. Vibration powder dispensing involves positioning a capillary tube at the bottom of a powder hopper that will not allow flow under static conditions, then applying suitable vibration to dispense powder. Experimental and discrete element method simulation work will be performed to assess the effects of capillary size, hopper incline and vibration parameters on the outlet mass flow rate of 316L stainless steel powder.

Gravity-fed powder delivery uses an inclined surface or tube to direct the powder from the dispensing system to its desired location. Experimental and discrete element method simulation work will be performed to assess the effects of tube size, tube length, inclination and mass flow rate on the trajectory and spread of 316L stainless steel powder.

Desired outcomes of these experiments are a mass flow rate range of at least 1 – 5 g/min on a single vibrating capillary, 95% or better powder capture, and a reduced time to turn the powder flow on and off compared to a conventional system. Results show that the system is capable of consistent mass flow rates between 0.6 and 7.9 g/min, 95% powder capture efficiency and lower on and off times than the conventional system, meeting all research goals.

2. Introduction

Additive manufacturing (AM) processes create parts by joining material together in the shape of a 3D model, typically layer by layer. Because there are many ways to accomplish this, the American Society for Testing and Materials (ASTM) devised a standard that divides the technologies into seven groups. Directed Energy Deposition (DED) is one of these [1].

2.1. Directed Energy Deposition Background

According to ASTM, directed energy deposition is “an additive manufacturing process in which focused thermal energy is used to fuse materials by melting as they are being deposited” [1]. To provide more detail, the following happen simultaneously to accomplish the DED process:

- The thermal energy source heats a small area on the substrate and melts material, forming a melt pool.
- Material is added to the melt pool and liquified.
- The substrate moves relative to the toolhead and material solidifies at the melt pool boundary as it moves away from the heat source.

The focused thermal energy can take the form of a laser beam, electron beam or plasma arc, and the material being deposited can be in the form of powder or wire. The system used in this research uses a laser as the thermal energy source and powder as the material, as shown in Figure 1 below. The figure also shows the argon shielding gas flow used to reduce oxidation on the solidified material.

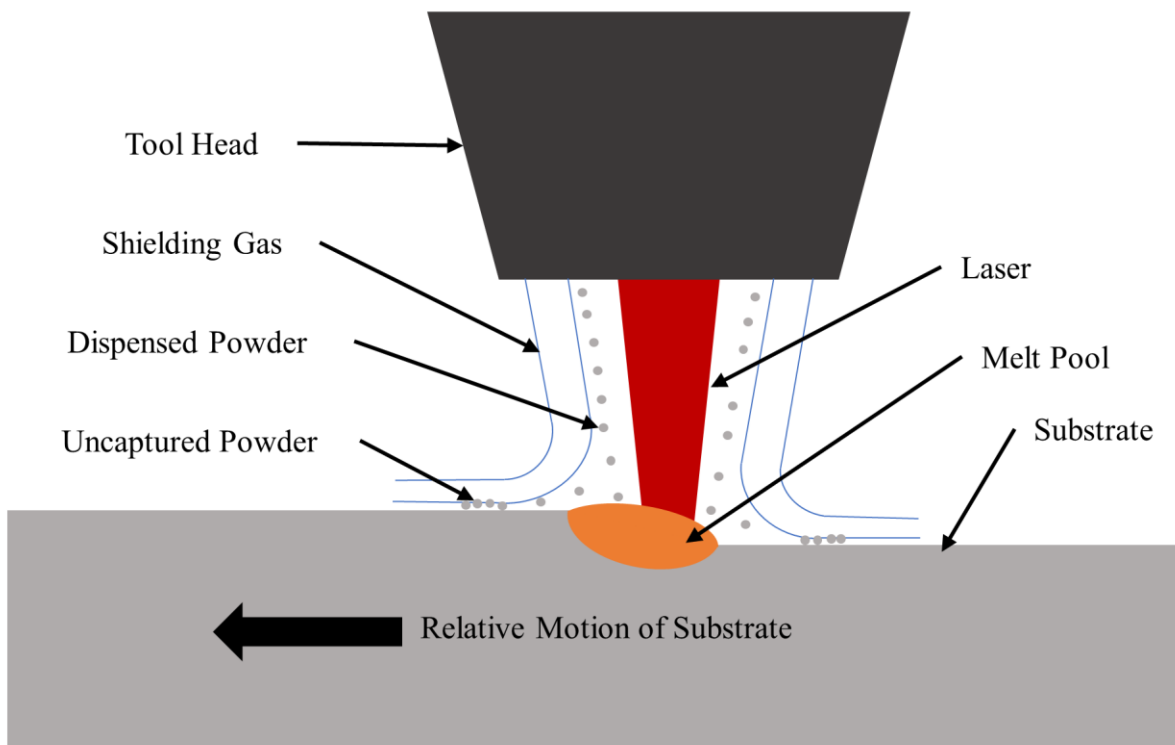


Figure 1: Directed Energy Deposition Process Diagram

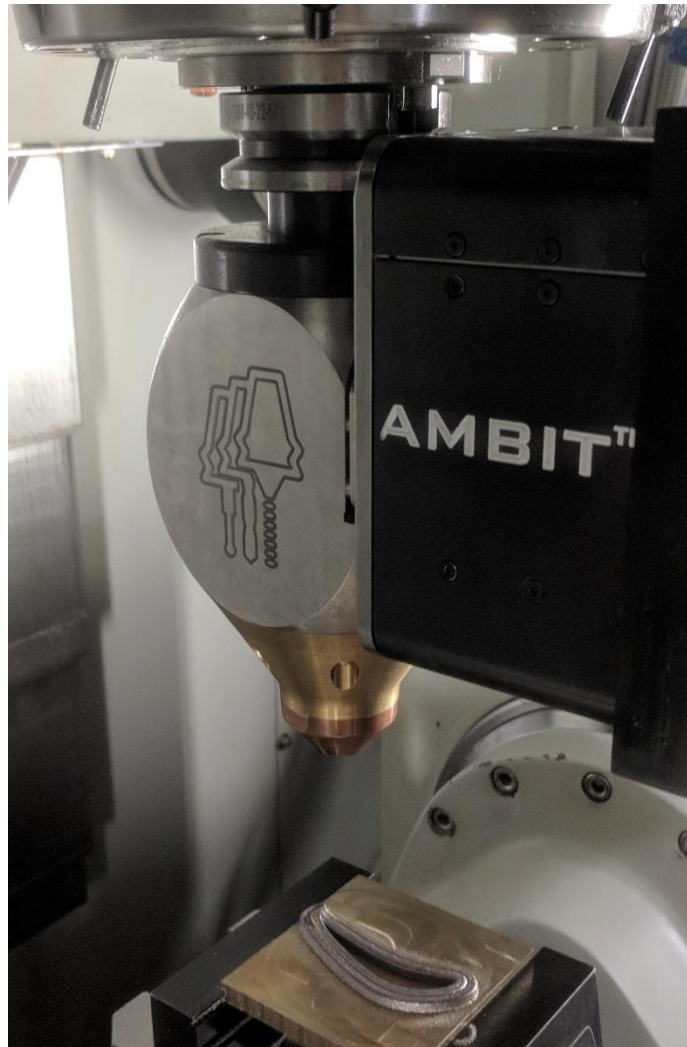


Figure 2: RIT Hybrid DED System

The DED process can work with any material that will melt and solidify, including metals, thermoplastics and ceramics. However, metals are by far the most common material used in the process. Thermoplastic parts can be made using many other conventional and AM processes. Ceramic materials are hard to process in many DED systems, and the resulting parts can have problems including high residual stress.

2.2. Applications

2.2.1. High-performance Parts

The most basic use case of DED systems is making high-performance parts out of a single material. The performance level of the part can come from the part's geometry, material, or both. DED systems are often implemented in a 5-axis configuration, allowing complex near-net shape parts to be built with no support structure. DED systems can work with materials that are difficult to process using other methods like machining, including stainless steels, tool steels, titanium alloys, nickel alloys and others.

2.2.2. Repair and Remanufacture

The DED process is well suited to being incorporated with other manufacturing methods like machining, often in the same work envelope/machine. Because of this, repair and remanufacturing of high-value components is possible. Such a process would have these general steps:

- The damaged part is inspected by automatic metrology equipment.
- A control system determines which areas are damaged and will be repaired.
- A machining process cuts away the damaged area.
- The cut away areas have material replaced using DED, adding slightly more material than the final part requires.
- The part is cut to the final dimensions and undergoes final inspection.

2.2.3. Multi-material Parts

The way material is added in the DED process allows any number of materials to be combined simultaneously. There are two ways to utilize this capability: in-situ alloying and functional gradients. In-situ alloying involves combining two or more feedstocks made of a single element or basic alloy into a more complex alloy. Some materials are difficult or impossible to make using other methods. A gradual change in the composition of a part across some portion of its volume is called a functional gradient. This allows the part to have different material properties in different areas.

2.3. Conventional Powder Delivery Background

A common system design for powder delivery in DED systems consists of a hopper, a metering device, a tube for delivery and a nozzle as shown in Figure 3. The hopper stores the powder in a sealed chamber to prevent moisture from affecting the powder and may be heated. The metering device takes powder from the hopper and sends it to the delivery tube at a set rate. A disk-type metering system has a channel that fills with powder as the disk rotates. The hopper and metering device are typically located outside the main DED machine, so the delivery tube must be relatively long, usually several meters. A gas stream is used to move the powder through the delivery tube. At the end of the delivery tube, the gas and powder both exit the nozzle directed at the melt pool. Nozzle designs include discrete tubes and a coaxial annulus.

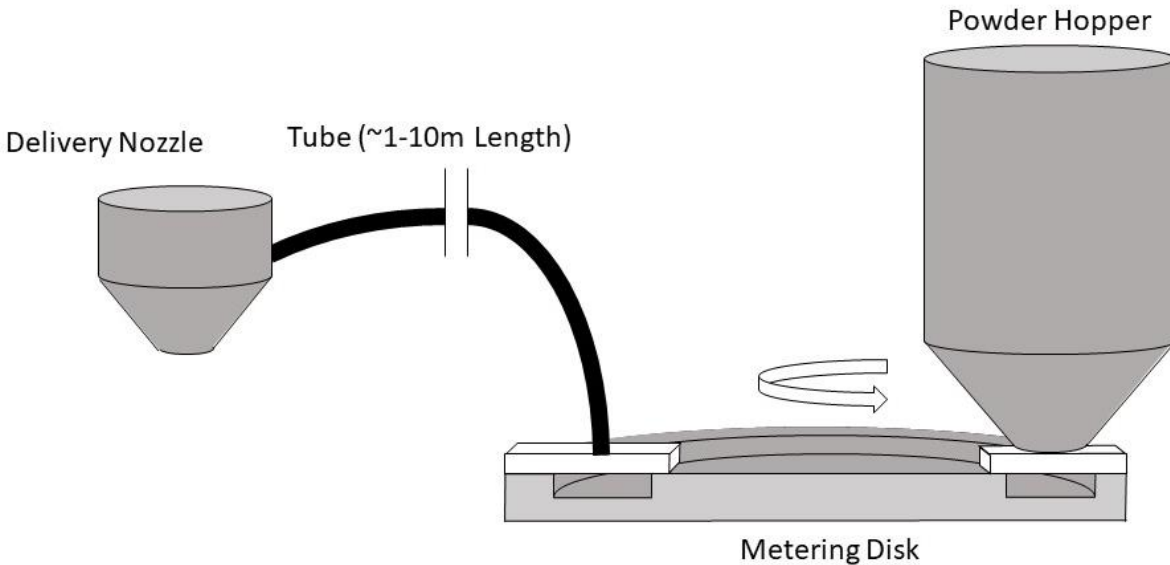


Figure 3: Conventional Powder Delivery System

2.4. Issue 1: Powder Capture Efficiency and Cost

Powder capture efficiency, $\eta_{capture}$, is the ratio of the mass of powder captured during printing, $m_{printed}$, to the total mass dispensed, $m_{dispensed}$.

$$\eta_{capture} = \frac{m_{printed}}{m_{dispensed}} \quad (1)$$

With conventional DED powder delivery systems, the powder capture efficiency is lower than 100% and can vary significantly between systems, process conditions and part geometry. Typical values are in the range of 10-70% [2-5] (see Section 3.2). In many systems, it is impractical or impossible to reuse powder that is not captured; it becomes waste. Both the gas flow that moves the particles and the velocity of the particles themselves contribute to lower powder capture in conventional designs. This is discussed in greater detail in Section 3.2.

To demonstrate the significance of powder capture efficiency in the operating costs of a DED system, consider the following example:

- A customer orders 1000 kg of parts made from Ti6Al4V.
- The process has a powder capture efficiency of 50%.
- The raw powder costs \$250 /kg.
- The machine uses 5 kW of power and electricity costs \$0.12 /kWh.
- The machine can build at 10 g/min (0.6 kg/hr).
- One operator is paid \$30 /hr to run the machine.

The operating costs for this scenario are broken down in Table 1.

Table 1: Operating Costs for Titanium Parts with 50% Powder Capture Efficiency

	Cost [\$]	Percent of Total [%]
Powder	500,000	90.7
Electricity	1,000	0.2
Labor	50,000	9.1
Total	551,000	100

Here, the powder is by far the largest part of the operating costs. If we change the scenario so that we use stainless steel powder costing \$50 /kg and our machine has 100% powder capture efficiency, we get the results shown in Table 2.

Table 2: Operating Costs for Stainless Steel Parts with 100% Powder Capture Efficiency

	Cost [\$]	Percent of Total [%]
Powder	50,000	49.5
Electricity	1,000	1.0
Labor	50,000	49.5
Total	151,000	100

These two scenarios illustrate two extremes of powder cost in a project, and in both cases the powder cost is a large portion of the operating costs. This means that developing ways to improve powder capture efficiency will provide significant cost savings for DED operation.

2.5. Issue 2: Composition Control and Multi-Material Parts

Powder capture efficiency with conventional powder delivery depends on many factors, including powder characteristics like density, size and shape. Different powders will have different powder capture efficiencies, even when all other factors remain constant. This makes building a part out of multiple materials simultaneously challenging because the ratio of the materials captured in the part can differ from the ratio of materials dispensed. While some success may be had using trial and error methods to compensate for the difference in captured composition, the best way to enable multi-material DED is by using a powder delivery system that gives total powder capture.

2.6. Issue 3: Powder Delivery Control Lag

Changing the mass flow rate of powders in real time during a build is useful for single material builds to achieve uniform layer height and for multi-material builds to locally vary composition. In a conventional powder delivery system, the powder must flow through several meters of tubing to reach the toolhead, which can take several seconds. Because of

this, control of the powder delivery rate to the melt puddle in real time is challenging. A system designed to dispense powder close to the toolhead will alleviate these problems.

2.7. Proposed System Design

To overcome the three issues discussed above, a powder delivery system with two independent parts is proposed. Vibration powder dispensing will give a low-velocity stream of powder with controllable mass flow rate. This will feed into a gravity-fed powder delivery system which will direct a concise, low-velocity stream into the melt pool.

2.7.1. Vibration Powder Dispensing

Vibration powder dispensing is based on using a capillary tube or similar opening at the bottom of a container of powder. If the capillary is properly sized, the powder will bridge and prevent discharge when no vibration is applied. Then, when vibration is applied, the contact forces between the particles are broken and the powder flows out. Applying vibrations with different amplitudes or frequencies can change the dispensed mass flow rate. A simple schematic showing a section view of a vibration powder dispensing system is shown in Figure 4.

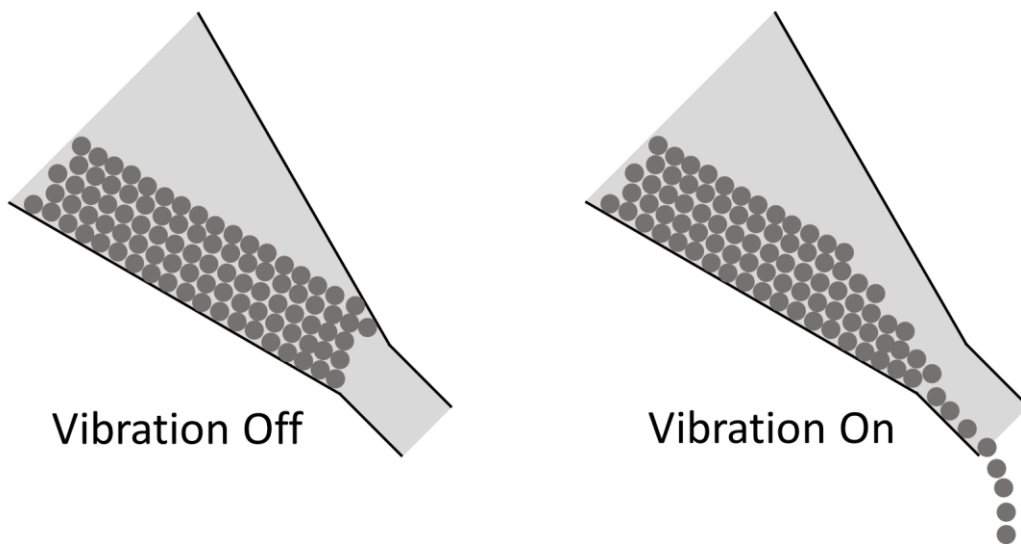


Figure 4: Vibration Powder Dispensing Cross Section View

2.7.2. Gravity-Fed Powder Delivery

With gravity-fed powder delivery, powder slides down an incline. Gravity is the only force accelerating the powder; no inert gas stream is necessary. For the purpose of this research, two geometries will be examined: a tube and a converging annulus. The tube geometry directs powder at the melt pool from one direction. Several tubes can be used to increase the mass flow rate or allow powder to be deposited from different sources. The annulus geometry directs powder at the melt pool from all directions. A simple schematic showing a section view of a gravity-fed powder delivery device is shown in Figure 5.

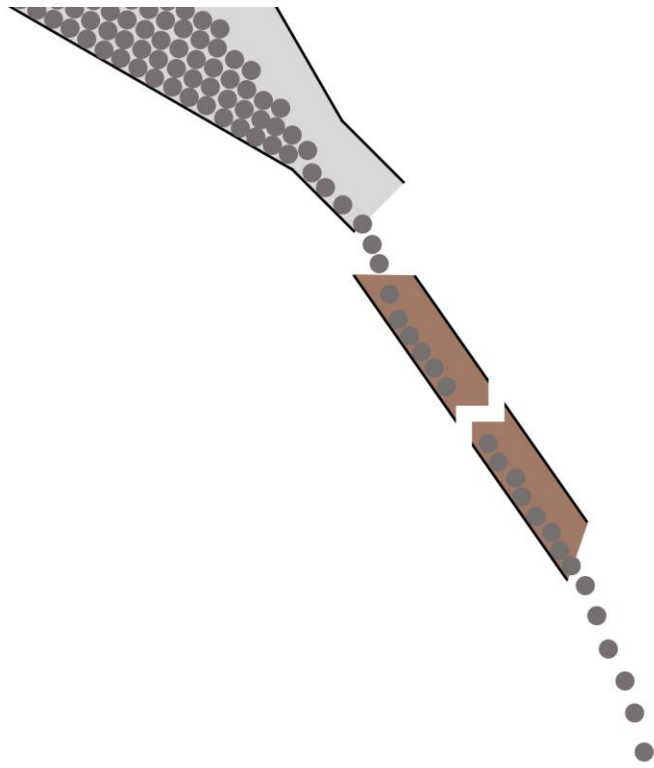


Figure 5: Gravity-Fed Powder Delivery Cross Section View

2.8. Research Questions

This research project will attempt to answer two primary questions related to powder delivery in directed energy deposition:

- Q1. Can a vibrating capillary tube dispense powder with a suitable range of rates and low enough variability for DED systems?
- Q2. Can powder fed by gravity down an inclined tube give near-total powder capture?

In addition, one secondary question will be answered:

- Q3. Can the proposed system significantly reduce the powder delivery control lag?

2.8.1. Question 1: Vibration Powder Dispensing Mass Flow Rate

Vibration powder dispensing enables gravity-fed powder delivery with no gas flow because the system can be small enough to be placed near the toolhead.

The first part of this question is the range of mass flow rates that can be achieved. This will be considered successful if the system can output 1 – 5 g/min of stainless steel powder. Higher mass flow rates can be achieved using two, three, or even four dispensing tools. This range is tailored to our machine using 316L stainless steel powder. Other systems with differently-sized laser beams and using different materials may require larger or smaller mass flow rates. The second part of this question is the variability in mass flow rate that can be achieved. A successful outcome will be a mass flow rate variability lower than that of the current system. The third and final aspect of this question is in the control mechanism for mass flow rate. For the sake of convenience, the mass flow rate should vary monotonically with a control parameter.

2.8.2. Question 2: Gravity-Fed Powder Delivery Capture Efficiency

Gravity-fed powder delivery enables the concise and low-velocity stream of powder necessary for reaching high powder capture efficiencies.

The proposed approach will be deemed successful if the system can achieve a 95% or better powder capture efficiency, as measured by printing single tracks with calibrated powder mass flow rates and comparing their actual and expected mass.

2.8.3. Question 3: Control Lag

With the greatly reduced distance the powder must travel, the time required for the powder to turn on and stabilize should be reduced. This question will be answered successfully if the powder delivery on and off times at the nozzle are lower than the current system.

3. Background and Literature Review

3.1. DED Process

The first DED process was the Laser Engineered Net Shaping (LENS) process developed by Sandia National Labs in 1997 [6] and commercialized by Optomec. Since then, companies including DMG Mori, Mazak, Trumpf, BeAM and others have released DED systems.

The estimated value of the metal additive manufacturing market in 2017 was \$800 million, of which powder DED makes up 21.6%. The expected compound annual growth rate for this market between 2017 and 2026 is 24.7% [7].

3.2. Conventional Gas Stream Powder Delivery

Powder metering units can give a large range of mass flow rate outputs, from about 1 – 100 g/min. Different configurations may be required to achieve this range. For example, the Oerlikon Twin 150 powder feeder used in our system can use spreader disks with cross sectional areas ranging from 0.6 – 51.2 mm². It should be noted that the mass flow rates here are for stainless steel powders, and because the flow rate setting is volumetric in nature, powders with significantly different densities will have proportionally different ranges of mass flow rates.

The mass flow rate that the delivery nozzle can handle has a maximum value. At some point, the amount of powder flowing through the nozzle will clog it. When designing a nozzle for a given process, there is a tradeoff between having a narrow nozzle that will direct the powder precisely and a wide nozzle that will allow high flow rates.

The variability in conventional powder delivery has not been reported frequently in the literature. Wang and Li [2] measured the mass flow rate of both a conventional and vibration powder dispensing system for an extended period and displayed the data in a figure. They reported the mean and variability of the vibration-based system, but not the conventional one. Visual estimation placed the relative standard deviation of the conventional system data between 1-2%. The variability of our Hybrid Manufacturing Technologies system is low when assessed using a linear fit technique. The coefficient of determination, R^2 , of a linear fit of mass dispensed versus time is over 0.999, indicating almost no deviation in flow rate.

Like variability, the on/off response time has not been reported frequently in the literature. Wang and Li [2] measured the response time to turn a conventional delivery system on and off, which was about 2-3 seconds. The on/off time of our system can be as low as about 2 seconds if the machine is configured correctly.

Capture efficiency values have been reported frequently in the literature. The range of values researchers have obtained is large due to the variations in machine design, process parameters and feedstock used. Several of these results are shown in Table 3.

Table 3: Summary of Powder Capture Efficiencies

Author(s)	Powder Capture Efficiency [%]
Katinas, Shang, Shin and Chen [3]	7.5
Unocic and DuPont [4]	0-14
Wang, Mei and Wu [5]	10-30
Wang and Li [2]	50
RIT Hybrid DED System	67

3.3. Vibration Powder Dispensing

A small number of authors have studied powder being dispensed out of a capillary tube using vibration. Such a system is described in Section 2.7.1. The basic results of authors who reported mass flow rate results as a function of vibration are summarized in Table 4 below. The goal of reviewing these studies is to find suitable system designs and parameters that will give useful mass flow rate control and low flow rate variability.

Looking at the results of all these studies, there are limited similarities. Depending on the powder properties and system design used in a study, the powder mass flow rate can increase, decrease, or increase then decrease with increasing vibration amplitude, frequency or acceleration. This disparity in behavior can be attributed to the wide range of powder properties, vibration settings and system designs used.

Several authors speculate that there are different powder flow regimes that occur at different vibration levels. Below a critical vibration level, there is no flow because the contact forces holding the powder in place have not been overcome. This phenomenon occurred in each case in which it was studied. Above the critical vibration level, flow begins to increase as vibration increases. In this regime, the interparticle contact forces are reduced, allowing more flow. At higher vibration levels, flow begins to decrease for some systems and reaches a constant value in other systems. In systems where the flow rate becomes constant, it is presumed that the interparticle contact forces are diminished to a constant level. In systems where the flow rate is reduced with increasing vibration, it is presumed that the vibration induces enough motion on the particles that interparticle contact forces are increased.

With regard to mass flow rate control, the studies done by Yang and Evans [8], [9] show promise. Their results show that the powder flow rate decreases monotonically with increasing vibration in a manner that should be easy to control. The ratio of maximum flow rate to minimum flow rate in their work was about 4 (~40 mg/s : 10 mg/s), a range that will suit most applications. The proposed system design and the powder used will follow the work of these authors to extend their results.

Variability of mass flow rate in vibration powder dispensing systems has been measured in several studies. Wang and Li [2] measured and reported that the variability in the mass flow rate was lower with their vibration powder dispensing system than with a conventional system. Chen, Seyfang and Steckel [10] measured the variability of mass flow rate in their vibration powder dispensing system and found that it was lower at lower

vibration amplitudes and frequencies and with sinusoidal waves instead of triangle or square waves.

The variability of mass output in dosing applications where a set mass is dispensed has been measured in other studies. Lu, Yang and Evans [11] found that applying vibration perpendicular to the capillary axis could achieve a relative standard deviation as low as 10%, while applying the vibration parallel to the capillary axis could achieve a relative standard deviation as low as 5%. This indicates that parallel vibration may give lower variability in mass flow rate. Lu, Yang and Evans [12] found that increasing vibration amplitude led to higher variability in dose mass in their experiments. This implies that higher vibration amplitude leads to higher variability in mass flow rate, although the authors note that the effects of starting and stopping the flow may play a significant part in the variability.

Table 4: Summary of Vibration Powder Dispensing Literature

Paper	Powder(s) Studied	Tube Size [μm]	Vibration Frequency [Hz]	Vibration Amplitude [μm]	Vibration Acceleration [m/s²]	Powder Flow Rate [mg/s]	Relationships
Matsusaka, Yamamoto and Masuda [13]	Alumina, D50 6 μm, irregular shape Alumina, D50 20 μm, irregular shape Alumina, D50 10 μm, spherical shape Fly-ash, D50 15 μm, spherical shape	400-1600	20-760	10-30 Transverse	1.1-684	0.05-6.5	Flow rate increases with vibration frequency, amplitude and acceleration
Yang and Evans [8]	H13 Tool Steel, < 212 μm, irregular shape	450	100-500	25-250 Transverse	40-395	10-70+	Flow rate decreases with vibration frequency, amplitude and acceleration
Kumar, Santosa, Beck and Das [14]	Soda-lime glass, 38 – 125 μm sieved into seven size ranges, spherical	100-2000	8-15k	? Transverse	?	3-14	Flow rate increases then decreases with increasing vibration frequency

Yang and Evans [9]	H13 Tool Steel, < 212 μm sieved into six size ranges, gas atomized Copper, 63 – 212 μm	380-600	50-300	~24-250 Transverse	16-315	8-50	Flow rate decreases with vibration frequency until about 200 Hz and decreases with amplitude
Jiang, Matsusaka, Masuda and Qian [15]	Fused Silica, 13.6 and 30.4 μm mass median PMMA, nine sizes from 5.2 to 58.2 μm mass median	1200	330	0-130 Transverse	0-559	0-90	Flow begins at a critical vibration acceleration, then increases to a peak and then decreases with increasing acceleration
Ishii, Suzuki, Segawa, Kihara, Yasuda and Matsusaka [16]	Zirconium Oxide, mixtures of 106 – 250 μm and < 45 μm , irregular shape Tungsten Oxide, mixtures of 106 – 250 μm and < 45 μm , nearly round shape	2000	280	0-80 Transverse	0-250	0-2000	Flow begins at a critical acceleration, then quickly reaches a stable value as acceleration increases

3.4. Models of Vibration Powder Dispensing

Analytical models of the phenomena experienced in vibration powder dispensing are challenging to construct. Due to the need to incorporate the effects of the mode of vibration, system geometry, and the stochastic nature of particle interactions, only relatively simple cases can be addressed this way.

Yang and Evans [17] studied the rate of powder flowing through a tube subject to transverse vibration. They assumed that particles are packed into an area of the tube and suspended by friction at the ends of the transverse movement. In between these ends, the particles fall subject to gravity when the friction force is overcome. This model neglects particle size distribution and variations in shape, as well as the complex force networks that result. The authors conclude that their model is useable in the range of 15 – 300 μm transverse amplitude and 100 – 200 Hz frequency when compared with experimental data taken with 25 – 250 μm H13 steel powder and a 450 μm diameter glass tube. They also speculate that their model does not fit well at higher vibrational energy levels because the random movement of particles becomes much more prevalent.

3.5. Previous Work with Proposed Approach

Wang and Li [2] designed, built and patented a system using vibration powder dispensing and gravity-fed powder delivery to feed a DED process. At the time of writing, they are believed to be the only researchers to implement and operate such a system. To summarize their study:

- 316L stainless steel powder with a size range from 45 – 105 μm was used.
- Three system designs were implemented: single stream, four stream and coaxial.
- Powder capture efficiencies up to 100% were obtained.
- Flow rate variability was lower and response time was faster for gravity-fed powder delivery than a conventional system.
- Porosity, surface roughness and oxidation in the parts made with gravity-fed powder delivery was lower than those made with a conventional system.

The authors did not identify any drawbacks of the system in their study, and there is clearly much to be gained. The authors did not study controlling the mass flow rate output of the system nor the ability to use multiple powders. These unexplored areas form the research questions presented in this proposal.

4. Modeling Background: Contact Mechanics and the Discrete Element Method (DEM)

While experimental work is crucial to answering the posed research questions, physics-based modeling can provide understanding at a deeper level and about things that would be difficult or impossible to do experimentally. As discussed in Chapter 3, the phenomena associated with powder moving through narrow passages with vibration is complicated and depends on many factors, which makes analytical and empirical modeling challenging. Again, the random nature of possibly sparse particles moving by sliding and/or bouncing down an inclined tube makes detailed analytical or empirical modeling difficult. For these reasons, the Discrete Element Method (DEM) is selected as a physics-based modeling tool to help gain deeper understanding of the particle behaviors in the system under study. The EDEM software package by Altair [18] is used for all work presented.

4.1. Calculations in DEM

In DEM, particle contacts, displacements, rotations and the resulting interactions are calculated at each simulation time step [19]. To prevent particles from affecting other particles they are not contacting and prevent numerical instability, the maximum allowable time step is the Rayleigh time step defined as

$$T_R = \frac{\pi R \sqrt{\rho/G}}{0.1613\nu + 0.8766} \quad (2)$$

where R is the particle radius, ρ is the particle density, G is the particle shear modulus and ν is the particle Poisson's Ratio. The equation's denominator is an approximation of a more complex implicit function as described in [20]. At each time step, the following take place: the domain is discretized, cells with particles are activated, contacts are checked, forces are calculated, and particle velocity and position are updated. The domain is usually discretized with a grid size 3-5 times that of the minimum particle radius. Each grid cell with particles is marked active, then active cells are searched for contacts. Contact occurs when the distance between particle centers is less than the sum of their radii because all particles are modeled as spheres. For contacting particles, the resulting forces are calculated using the equations prescribed in the contact model. For each particle, the sum of the forces and moments acting on it are used to calculate its acceleration, velocity, and position.

Particles are added to the simulation domain using geometries designated as "factories." A particle factory can create particles from a specific material at a specified rate and with initial properties like velocity at set times. The initial properties can be fixed, random or selected from a distribution. Particles are removed from the simulation when they move outside of the domain.

4.2. Powder in DEM

All particles modeled in EDEM are spheres or composite shapes made of spheres, allowing for the approximation of complex and irregular geometries. Several particle geometries can be defined, each with a specified size range and distribution. When powder is inserted into

the model, each particle geometry is created at the specified frequency. Thus, a close approximation of a real batch of powder is created.

Measurements of real powder must be taken in order to create a realistic and useful approximation in a simulation. The values that need to be found are the mean size, size distribution, and various shapes and their relative frequencies. To achieve this, image analysis is useful, automated or not. Images of powder will give a particle's size and shape, and when a large enough sample of size and shape data is collected, the size distribution can be calculated. Shape is often left to human decision, for instance, sorting into several predefined categories (e.g., round, oblong, satellite).

4.2.1. Powder Size and Shape Measurement

A sample of the powder used in this work, LPW gas atomized 316L stainless steel, was spread into a sparse monolayer, then imaged using a scanning electron microscope. Figure 6 shows one of these images, and Figure 7 shows a thresholded version of the same image which was used to extract and measure 2D particle outlines. Six such images were analyzed, resulting in a total of about 1000 particle profiles being analyzed.

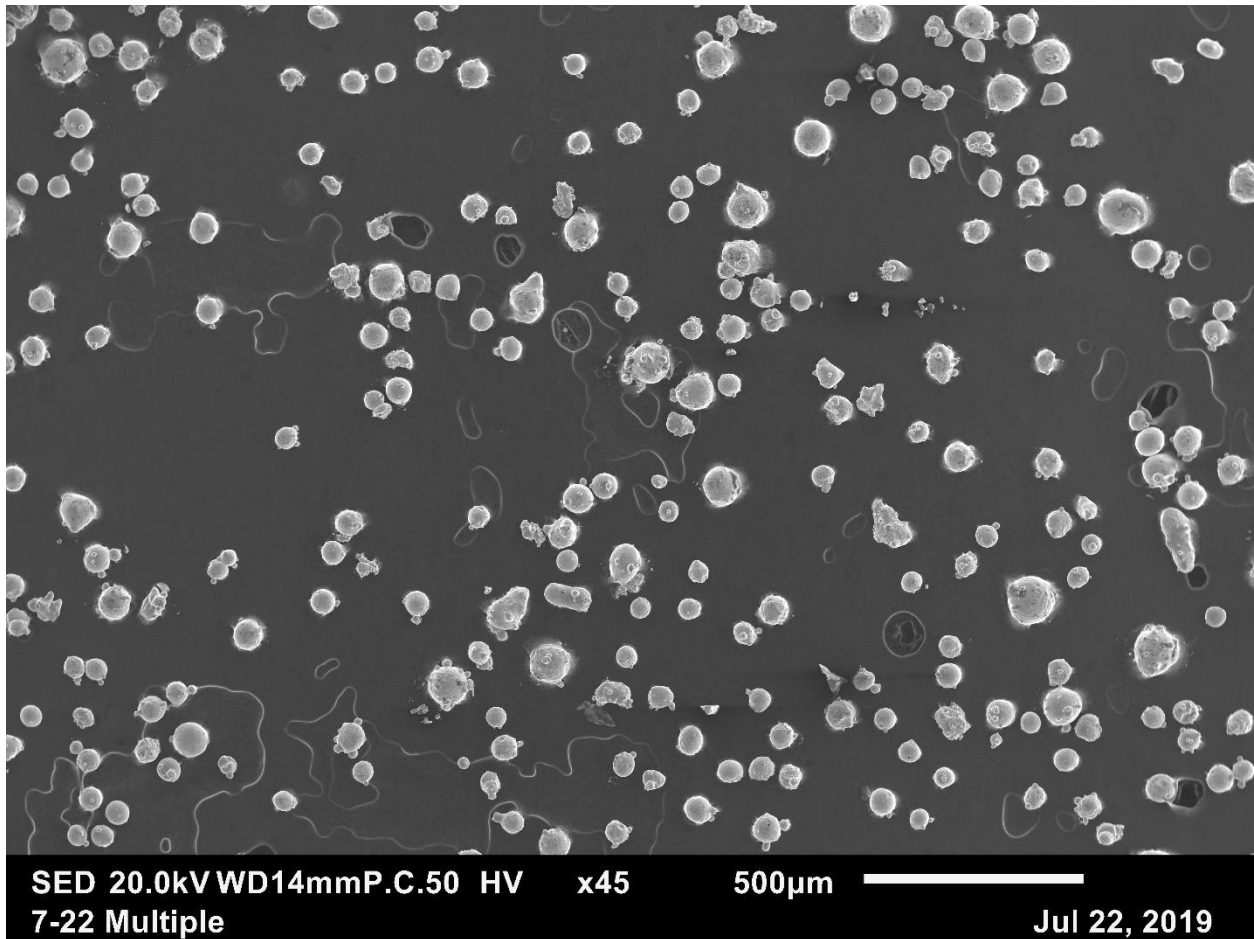


Figure 6: SEM Image of Powder Particles

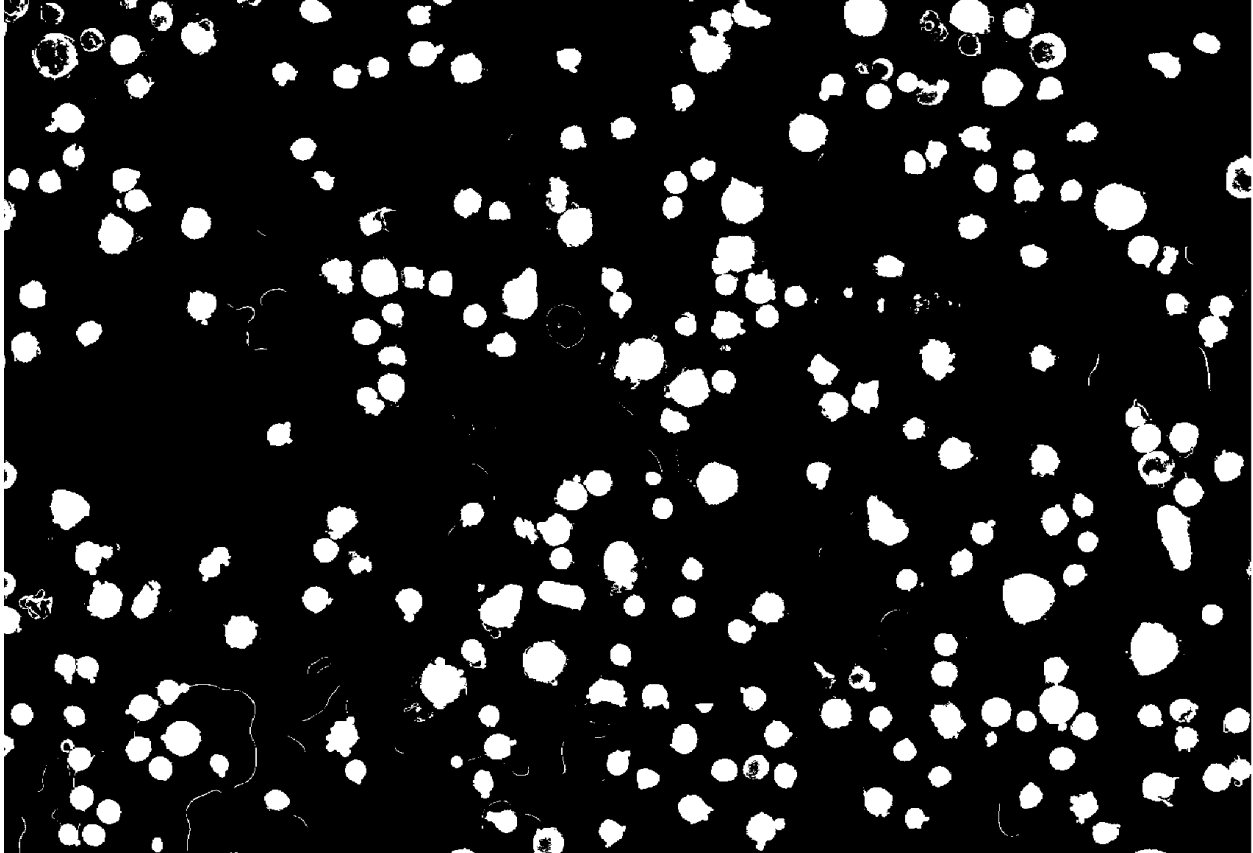


Figure 7: Processed Image of Powder Particles

It is important to note that some particle shapes would be difficult to accurately measure and replicate using this 2D measurement technique. For instance, oblate ellipsoids with axis lengths a , b and c where $a \approx b > c$ (tending toward disc-like) would tend to lay flat on the substrate during imaging, and their thickness could not be easily measured. However, this gas atomized powder has roughly spherical and prolate ellipsoid shaped particles with axis lengths a , b and c where $a \approx b < c$ (tending toward rod-like). We can approximate an imaged particle's thickness by revolving the image around the longest dimension.

With this initial observation of particle shape, the imaged particles were measured and sorted using MATLAB [21]. In order to be included in the size distributions, an imaged particle needs to meet the following criteria:

- An area between 1500 – 50000 pixels.
- A circularity greater than or equal to 0.3. Circularity is calculated as the ratio of the image area in pixels to the area calculated using the particle perimeter. A perfect circle has the maximum circularity of 1.0.
- A minimum Feret diameter greater than or equal to 40 μm and a maximum Feret diameter less than or equal to 160 μm . The Feret diameter is the measurement a pair of calipers would give at a certain orientation of the image.

The results to be used in DEM simulations are the two particle shapes shown in Figure 8, each with its own size distribution as shown in Table 5. Spherical particles were based on a

single template particle with a radius of 70 μm and made up 73.4% of the mass. Oblong particles were based on a template particle with two 50.9 μm radius particles with centers 50.9 μm apart and made up the remaining 26.6% of the mass. The template particles' radii are scaled by the relative size in Table 5 with a frequency according to the mass fraction to approximate the size distributions.

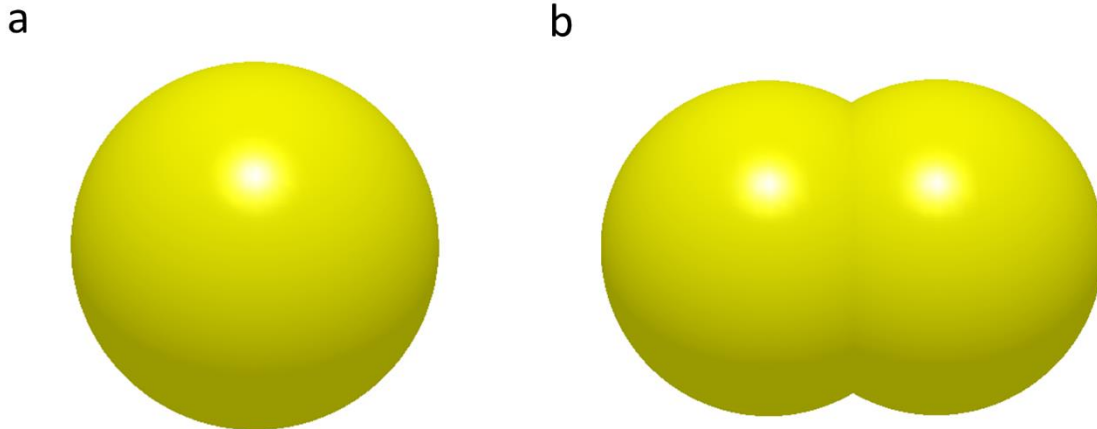


Figure 8: DEM Particle Shapes a) spherical b) oblong

Table 5: Measured Particle Size Distributions

Spherical Particles		Oblong Particles	
Relative Size	Mass Fraction	Relative Size	Mass Fraction
0.3571	26.7640	0.4111	7.4380
0.4286	32.3601	0.4765	21.4876
0.5000	16.5450	0.5420	19.4215
0.5714	8.8808	0.6074	14.4628
0.6429	6.5693	0.6728	15.2893
0.7143	4.7445	0.7383	7.4380
0.7857	3.1630	0.8037	5.7851
0.8571	0.7299	0.8691	4.9587
0.9286	0.1217	0.9346	2.8926
1.0000	0.1217	1.0000	0.8264

4.3. Forces and Contact Models in DEM

4.3.1. Particle-Particle Contacts Using the EEPA Model

The Edinburgh visco-Elastic-Plastic Adhesive (EEPA) contact model is used for powder-powder material interactions in EDEM [22]. It accounts for contact forces arising from both elastic and plastic deformation of the particles, the area-dependent adhesive forces acting on the particles and the time-dependent damping forces while contacting particles are moving. Rolling friction may also be present if the particles rotate.

The forces present when two spheres are in contact are shown in Figure 9. The normal force acts perpendicular to the contact in a direction away from the contact. The adhesive force acts perpendicular to the contact in a direction toward the contact. The tangential friction force acts parallel to the contact. The rolling friction force acts parallel to the contact.

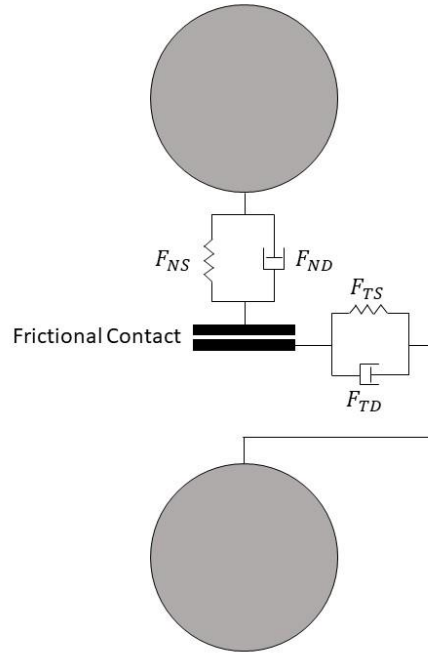


Figure 9: Contact Model Schematic

A summary of the equations used in the model is paraphrased here from [22]. The normal contact force, F_N , is the sum of the hysteretic spring force, F_{NS} , and the visco-elastic damping force, F_{ND}

$$F_N = F_{NS} + F_{ND} \quad (3)$$

The hysteretic spring force accounts for non-linear contact forces arising from elastic deformation, plastic deformation and adhesion

$$F_{NS} = \begin{cases} F_0 + k_1 \delta^n & \text{if } k_2(\delta^n - \delta_p^n) \geq k_1 \delta^n \\ F_0 + k_2(\delta^n - \delta_p^n) & \text{if } k_1 \delta^n > k_2(\delta^n - \delta_p^n) > -k_{adh} \delta^x \\ F_0 - k_{adh} \delta^x & \text{if } -k_{adh} \delta^x > k_2(\delta^n - \delta_p^n) \end{cases} \quad (4)$$

where F_0 is the constant pull-off force, k_1 is the initial stiffness, k_2 is the unloading/reloading stiffness, k_{adh} is the adhesion stiffness, δ is the displacement, δ_p is the plastic displacement, n is the power value for the mechanical stiffness relationships and x is the power value for the adhesion stiffness relationship. The first portion of the equation describes the behavior when the contact is loaded for the first time or when it is reloaded past its previous peak load. The second portion describes the behavior when the contact is unloaded or reloaded below the peak load. The third portion describes the behavior when the contact is separated but adhesive forces are still present. There is no memory of plastic deformation, so once a contact is broken, subsequent contacts will behave like new contacts. This model will create a friction force from a separated contact with adhesive force, which is useful for modeling adhesive phenomena as well as surface roughness effects not captured by the particle's smooth geometry.

The normal damping force, F_{ND} is given by

$$F_{ND} = \begin{cases} \beta_L V_N & \text{if } n = 1 \\ -2 \sqrt{\frac{5}{6}} \beta_{NL} \sqrt{K_N m^*} V_N & \text{if } n > 1 \end{cases} \quad (5)$$

where V_N is the relative normal velocity, β_L is the linear damping coefficient, β_{NL} is the non-linear damping coefficient, K_N is the Hertzian normal stiffness and m^* is the equivalent mass.

$$\beta_L = \sqrt{\frac{4m^*k_1}{1 + \left(\frac{\pi}{\ln e}\right)^2}} \quad (6)$$

$$\beta_{NL} = \frac{\ln e}{\sqrt{\ln^2 e + \pi^2}} \quad (7)$$

$$K_N = 2E^* \sqrt{R^*} \delta \quad (8)$$

$$m^* = \frac{m_1 m_2}{m_1 + m_2} \quad (9)$$

where m_1 and m_2 are the masses of the two particles in contact, E^* is the equivalent Young's modulus of the two particles, R^* is the equivalent radius of the two particles and e is the coefficient of restitution.

$$\frac{1}{R^*} = \frac{1}{R_1} + \frac{1}{R_2} \quad (10)$$

$$\frac{1}{E^*} = \frac{1-\nu_1}{E_1} + \frac{1-\nu_2}{E_2} \quad (11)$$

where R_1 and R_2 are the radii, ν_1 and ν_2 are the Poisson's ratios and E_1 and E_2 are the elastic moduli of the two particles.

The tangential force is frictional in nature and obeys Coulomb's friction criteria. As with the normal force, it is the sum of the spring and damping type forces

$$F_T = \begin{cases} F_{TS} + F_{TD} & \text{for } F_T \leq \mu_k F_{NS} \\ F_{TC} & \text{for } F_T > \mu_k F_{NS} \end{cases} \quad (12)$$

where F_{TS} is the tangential spring force, F_{TD} is the tangential damping force, F_{TC} is the critical tangential force and μ_k is the kinematic coefficient of friction. F_{TC} is the maximum tangential force value that can be obtained in static contact and is defined as

$$F_{TC} = \mu_s |F_{NS} + k_{adh} \delta^x - F_0| \quad (13)$$

where μ_s is the static coefficient of friction. This equation will only give the normal force components that act upon two particles while they are in contact and represents the maximum tangential force that is possible before motion occurs.

Below the limit of F_{TC} , the tangential spring and damping forces are added to give the total tangential force. F_{TS} is calculated incrementally

$$F_{TS} = F_{TS(n-1)} + k_T \Delta \delta_T \quad (14)$$

where $F_{TS(n-1)}$ is the tangential spring force at the previous time step, k_t is the tangential stiffness and $\Delta \delta_t$ is the change in tangential displacement. The tangential stiffness is related to the normal stiffness by ζ_{TM} such that

$$k_T = \zeta_{TM} \begin{cases} k_1 & \text{if } n = 1 \\ 8G^* \sqrt{R^* \delta} & \text{if } n > 1 \end{cases} \quad (15)$$

where ζ_{TM} is the tangential stiffness multiplier and G^* is the equivalent shear modulus.

The tangential damping force is described as

$$F_{TD} = \begin{cases} -\beta_{TL} V_T & \text{if } n = 1 \\ -2 \sqrt{\frac{5}{6}} \beta_{NL} \sqrt{k_T m^*} V_T & \text{if } n > 1 \end{cases} \quad (16)$$

where V_T is the relative tangential velocity and β_{TL} is the linear tangential damping coefficient,

$$\beta_{TL} = \sqrt{\frac{4m^* k_T}{1 + \left(\frac{\pi}{\ln e}\right)^2}} \quad (17)$$

Lastly, the rolling friction is described in terms of the applied torque as

$$\tau_i = -\mu_r F_{NS} R_i \frac{\omega_i}{|\omega_i|} \quad (18)$$

where τ_i is the torque applied to particle i , μ_r is the coefficient of rolling friction, R_i is the distance from the contact point to the center of mass of particle i , and ω_i is the rotational velocity of particle i at the contact point.

4.3.2. Material Properties in the EEPA Contact Model

When defining a study using the Edinburgh model, the following material properties must be specified [22]. Coefficients of friction and coefficients of restitution must be specified for all material pairs that exist in a system, including a material interacting with the same material.

- Constant Pull-Off Force, F_0 [N]: Used to model constant forces in the system including van der Waals and electrostatic forces.
- Meso-Contact Adhesion Energy, $\Delta\gamma$ [J/m²]: Used to calculate the adhesive force between two particles when the contact is unloaded and about to separate, F_{min}

$$F_{min} = \pi\Delta\gamma\psi a \quad (19)$$

where ψ is the adhesion constant, usually assumed to be 3/2, and a is the contact patch radius. When the model separates, a plastic contact down to F_{min} , k_{adh} can be calculated as

$$k_{adh} = \frac{F_{min} - F_0}{\delta_{min}^x} \quad (20)$$

- Contact Plasticity Ratio, λ_p : The contact plasticity ratio relates the virgin loading stiffness k_1 to the unloading/reloading stiffness k_2 by

$$\lambda_p = \left(1 - \frac{k_1}{k_2}\right) \quad (21)$$

- Power Value for Stiffness, n : Allows for non-linear behavior in the normal contact force.
- Power Value for Adhesion, x : Allows for non-linear behavior in the adhesive force.
- Tangential Stiffness Multiplier, ζ_{TM} : Relates the tangential stiffness to the normal stiffness. Typically set between 2/3 and 1 [22].
- Coefficient of Static Friction, μ_s : Relates normal force to frictional force in a static system. Must be specified for every material pair.
- Coefficient of Rolling Friction, μ_r : Relates normal force to rolling resistance. Must be specified for every material pair.
- Coefficient of Restitution, e : Ratio of relative velocity between particles before and after collision. Lower values indicate more kinetic energy is transformed to another form during collision.
- Shear Modulus, G [MPa]: Shear stiffness. Must be specified for every material. The elastic Modulus E is derived from this using the relation $E = 2G(1 + \nu)$.

- Poisson's Ratio, ν : Ratio of axial to transverse deformation. Must be specified for every material.
- Density, ρ [kg/m^3]: Must be specified for each material.

4.3.3. Particle-Equipment Contacts using the Hertz-Mindlin with JKR Adhesion Model

The Hertz-Mindlin contact model with Johnson-Kendall-Roberts (JKR) Adhesion is similar to the previously discussed EEPA model, but simpler. Each contact is modeled with a normal and tangential force, each of which have an elastic and damping component.

The total normal force, F_N is the sum of the elastic and damping components. The elastic normal force is defined as

$$F_{NE} = -4\sqrt{\pi\gamma E^*} a^{\frac{3}{2}} + \frac{4E^*}{3R^*} a^3 \quad (22)$$

$$\delta = \frac{a^2}{R^*} - \sqrt{\frac{4\pi\gamma a}{E^*}} \quad (23)$$

where the equivalent Young's Modulus E^* and the equivalent contact radius R^* are defined the same way as in the EEPA model. The surface energy parameter γ allows for contact forces greater than zero when the particles are close but not in contact.

The damping normal force is defined as

$$F_{ND} = -2\sqrt{\frac{5}{6}}\beta\sqrt{K_n m^*} v_n^{rel} \quad (24)$$

where the normal stiffness K_n , the equivalent mass m^* and the normal relative velocity v_n^{rel} are defined the same way as in the EEPA model. The constant β is defined as

$$\beta = \frac{\ln e}{\sqrt{\ln^2 e + \pi^2}} \quad (25)$$

The total normal force, F_T is the sum of the elastic spring and damping components. The elastic tangential force is defined as

$$F_{TE} = -K_t \delta_t \quad (26)$$

where δ_t is the tangential overlap, and the tangential stiffness K_t is defined as

$$K_t = 8G^*\sqrt{R^*\delta_n} \quad (27)$$

where G^* is the shear modulus defined in the same way as the EEPA model.

The damping tangential force is defined as

$$F_{TD} = -2\sqrt{\frac{5}{6}}\beta\sqrt{K_t m^*} v_t^{rel} \quad (28)$$

with the tangential relative velocity v_t^{rel} . The total tangential force is limited by friction such that the maximum is

$$F_T \leq \mu_s F_N \quad (29)$$

4.3.4. Material Properties in the Hertz-Mindlin with JKR Adhesion Contact Model

In this work, the Hertz-Mindlin with JKR Adhesion contact model was used for modeling particle-equipment contacts. The following parameters must be calibrated and specified for each equipment material as it interacts with the one powder material used.

- Surface Energy, γ [J/m²]: Allows contact force between particles when they are close but not touching.
- Coefficient of Static Friction, μ_s : Relates normal force to frictional force in a static system. Must be specified for every material pair.
- Coefficient of Rolling Friction, μ_r : Relates normal force to rolling resistance. Must be specified for every material pair.
- Coefficient of Restitution, e : Ratio of relative velocity between particles before and after collision. Lower values indicate more kinetic energy is transformed to another form during collision.
- Shear Modulus, G [MPa]: Shear stiffness. Must be specified for every material. The elastic Modulus E is derived from this using the relation $E = 2G(1 + \nu)$.
- Poisson's Ratio, ν : Ratio of axial to transverse deformation. Must be specified for every material.
- Density, ρ [kg/m³]: Must be specified for each material.

4.4. Calibrating a Material in DEM

The size, shape and contact model properties of the simulated material(s) must be measured and calibrated. Often, the actual micro-scale contact property is not measured or desirable as a model input. Replicating the bulk behavior of the material in a representative system is the aim of this calibration work.

As described in Section 4.3, there are two separate contact models used in this work, particle-particle and particle-equipment. Both are modeled differently and have different parameters that require calibration.

4.4.1. Initial Properties

For the particle-particle contact model, some initial contact model values were set using values found in the literature. The values of Poisson's ratio and bulk density were taken from [23]. Coefficient of restitution was set following the work in [24]. The shear modulus was set following the recommendations of [25, 26]. Coefficient of static friction was set at 0.6 as a midpoint between the EDEM default of 0.8 and the 0.4 from [27]. Coefficient of rolling friction was set to 0.1 to account for the large amount of satellite particles present in

the powder. The remaining parameters were set to EDEM default values. The initial properties are shown in Table 6.

Table 6: Initial Properties for Particle-Particle Contact Model

Property	Value
Poisson's Ratio	0.25
Solids Density [kg/m ³]	7990
Shear Modulus [MPa]	1
Coefficient of Restitution	0.7
Coefficient of Static Friction	0.6
Coefficient of Rolling Friction	0.1
Constant Pull-Off Force [N]	0
Surface Energy [J/m ²]	0
Contact Plasticity Ratio	0.5
Slope Exponent	1.5
Tensile Exponent	1.5
Tangential Stiffness Multiplier	0.667

There are two equipment materials used in simulations, a stainless steel material in vibration powder dispensing and a copper material in gravity-fed powder delivery. For both materials, the density, Poisson's ratio, shear modulus and coefficient of rolling friction were left at the default values seen in Table 7. The values for coefficient of restitution, coefficient of static friction and surface energy were calibrated.

Table 7: Initial Properties for Particle-Equipment Contact Model

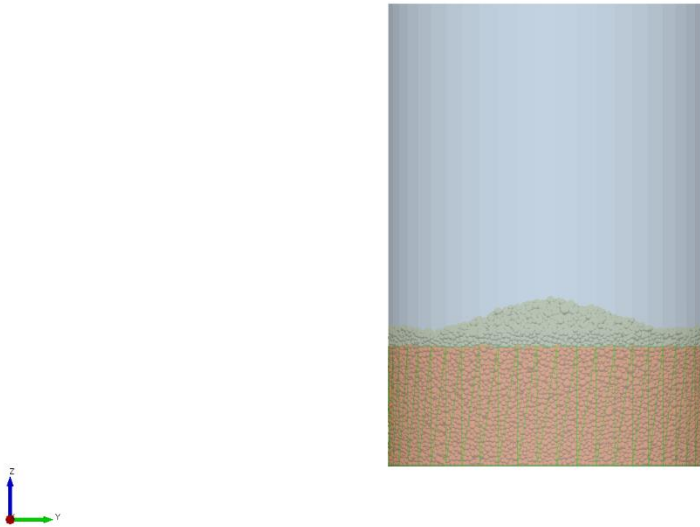
Property	Value
Poisson's Ratio	0.25
Density [kg/m ³]	2500
Shear Modulus [MPa]	100
Coefficient of Rolling Friction	0.01
Coefficient of Static Friction	0.8
Coefficient of Restitution	0.5
Surface Energy [J/m ²]	0

4.4.2. Particle Bulk Density

Because the particle packing and other factors may not precisely match the real material, the bulk material density may need to be calibrated such that the simulation material matches the apparent density of the real material. The apparent density of the real material was measured following ASTM B212-17 [28] and found to be 4140 kg/m³ (cup volume 25.01 cm³). To measure and calibrate the apparent density in EDEM, a 4 mm cylinder was

filled with 0.1 g (~100,000 particles) of powder using a 2.54 mm diameter powder factory 25 mm above it. This resulted in an apparent density of 4527 kg/m³, and the bulk solids density was adjusted to 7300 kg/m³.

Time: 0.711403 s



Altair EDEM™

Figure 10: Bulk Density Calibration Simulation

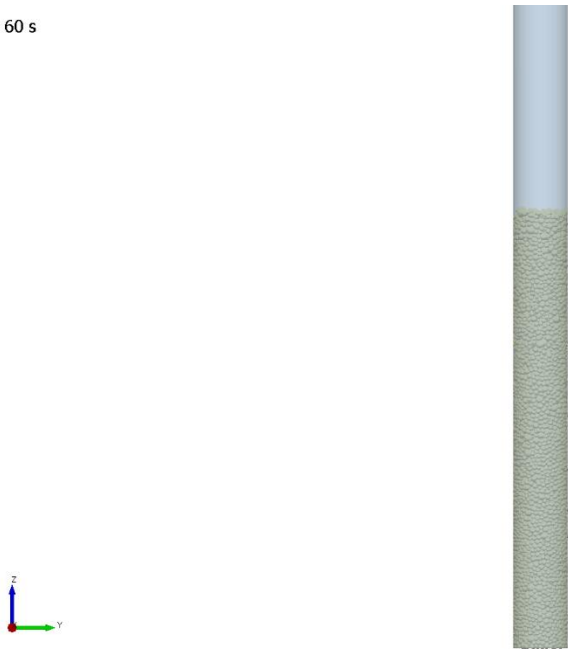
4.4.3. Tapped Density and Particle-Particle Coefficient of Static Friction

The tapped density test subjects a column of powder to repeated impacts and measures how much it compresses, which is strongly correlated with the static coefficient of friction. Experimental measurements were made following ASTM B527-15 [29]. The experimental final density was found to be 4.87 g/cm³.

The simulation setup consisted of 0.01 g of powder (~10,000 particles) in a 0.347 mm diameter cylinder which was subjected to the following kinematics for 1 minute (250 cycles):

- The cylinder was held stationary for 0.06 s.
- The cylinder was moved upward at a constant velocity of 16.67 mm/s for 0.18 s.
- The cylinder was allowed to free fall a distance of 3 mm for 0.0247 s subject to normal gravity.

Time: 60 s



Altair EDEM™

Figure 11: Tapped Density Calibration Simulation

After correcting for edge effects due to the small number of particles, it was found that the final density of the material on the cylinder best fit the experimental results when the coefficient of static friction was set to 0.4.

4.4.4. Static Angle of Repose and Particle-Particle Coefficient of Rolling Friction

The static angle of repose measures the angle of a slope formed on the edge of a pile of powder at rest. Two material properties that most significantly affect the static angle of repose are the static coefficient of friction and coefficient of rolling friction. As the coefficient of static friction was previously calibrated, the coefficient of rolling friction can be calibrated.

No standard exists for experimental measurement of static angle of repose. The procedure used is as follows:

- The flat bottom surface of the density cup used in ASTM B212-17 is positioned about 25 mm underneath a Hall flow funnel.
- An amount of powder sufficient to fully cover the cup surface is run through the funnel and left in a pile on the cup surface.
- The height of the pile is measured.
- The static angle of repose is calculated using the height, h and diameter, D of the pile as

$$\text{Static Angle of Repose} = \tan^{-1} \left(\frac{2h}{D} \right) \quad (30)$$

The measured value of static angle of repose is 30.2 degrees.

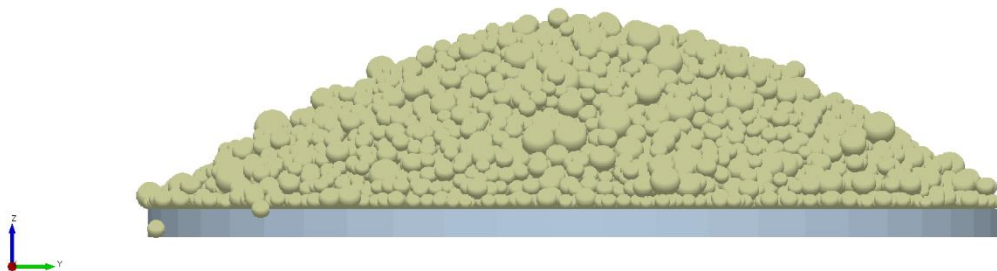
The simulation setup for calibrating the static angle of repose consists of a 0.4 mm diameter powder factory situated 2 mm above a 3 mm diameter plate. Each simulation generated 2E – 5 kg of powder (about 20,000 particles) at a rate of 1E – 5 kg/s.

Four simulations were run using the levels of coefficient of static and rolling friction shown in Table 8. While the coefficient of static friction was previously calibrated, including it in this analysis allows insight into the relative sensitivity of the output to each factor and how much error in previous calibration could impact this one.

Table 8: Factors and Levels for Static Angle of Repose Calibration Simulations

	Coefficient of Static Friction	Coefficient of Rolling Friction
Level 1	0.25	0.05
Level 2	0.5	0.1

Time: 2.5 s



Altair EDEM™

Figure 12: Static Angle of Repose Calibration Simulation

Analyzing the results using multiple linear regression gave the static angle of repose as a function of both the coefficient of static (SCoF) and rolling friction (RCoF) as follows

$$\text{Static Angle of Repose} = 12.26 * \text{SCoF} + 97.06 * \text{RCoF} + 16.41 \quad (31)$$

Setting the static angle of repose to 30.2 degrees and the coefficient of static friction to 0.4 as previously calibrated resulted in a coefficient of rolling friction of 0.09.

4.4.5. Surface Adhesion and VPD Particle-Equipment Surface Energy

To calibrate the behavior of particles interacting with the stainless steel dispensing tip used in vibration powder dispensing, a less precise but still adequate approach was taken. A

monolayer of powder on a flat piece of stainless steel was gradually inclined to vertical, then tapped. It was observed that the majority of the powder began sliding when the steel plate was tilted at 60 to 75 degrees of inclination. A small fraction of powder remained in place at a vertical inclination; however, no powder remained after a light tap. This process was replicated in EDEM to calibrate the surface energy parameter that creates an adhesive force. A full factorial study consisting of four simulations varying coefficient of static friction and surface energy was run using the levels shown in Table 9.

Table 9: Factors and Levels for VPD Particle-Equipment Surface Energy Calibration Simulations

	Coefficient of Static Friction	Surface Energy (J/m²)
Level 1	0.5	0.0005
Level 2	0.8	0.0015

Time: 1.57 s

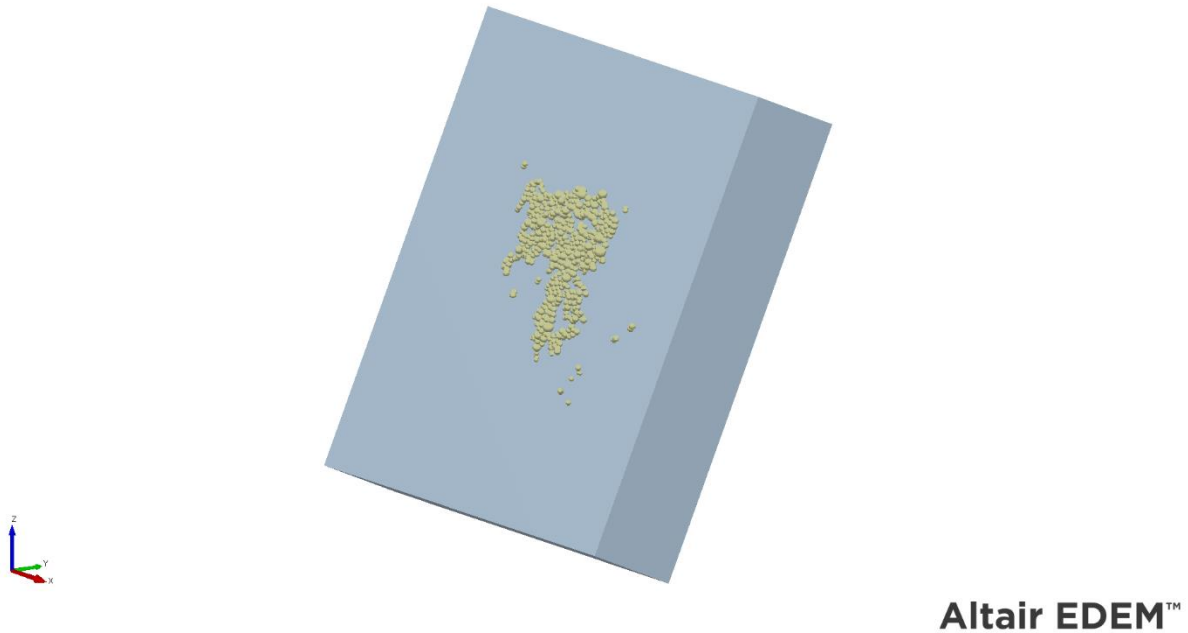


Figure 13: Equipment Adhesion Calibration Simulation

The simulation results showed a range of behavior that encompassed the experimentally observed behavior. The surface energy parameter was set to 0.001 J/m².

4.4.6. Particle-Particle Surface Energy

The particle-particle surface energy parameter is the last remaining parameter to be calibrated for the particle-particle interactions. For the purposes of this work, it was acceptable to calibrate this last parameter using a subset of the vibration powder dispensing experimental results. After some initial simulations to get an approximate value for the particle-particle surface energy, four simulations were run at two inclines and two surface energy levels. The mass flow rate values from these simulations were compared

with experimental results to select the final value of 0.006 J/m². The data is shown in Table 10.

Table 10: Particle-Particle Surface Energy Calibration Data

Dispensing Tip Incline [°]	Particle-Particle Surface Energy [J/m²]	Simulation Mass Flow Rate [g/min]	Experimental Mass Flow Rate [g/min]
42.5	0.004	9.5	7.95
22.5	0.004	1.6	1.15
42.5	0.006	8.0	7.95
22.5	0.006	1.4	1.15

4.4.7. Final DEM Contact Model Properties

After performing all these calibrations, the following contact model properties were decided on and used for the simulations of vibration powder dispensing and gravity-fed powder delivery.

Table 11: Final Particle-Particle Contact Model Properties

Property	Value
Poisson's Ratio	0.25
Solids Density [kg/m ³]	7300
Shear Modulus [MPa]	1
Coefficient of Restitution	0.7
Coefficient of Static Friction	0.4
Coefficient of Rolling Friction	0.09
Constant Pull-Off Force [N]	0
Surface Energy [J/m ²]	0.006
Contact Plasticity Ratio	0.5
Slope Exponent	1.5
Tensile Exponent	1.5
Tangential Stiffness Multiplier	0.667

Table 12: Final Particle-Equipment Contact Model Properties

Property	Value
Poisson's Ratio	0.25
Density [kg/m ³]	2500
Shear Modulus [MPa]	100
Coefficient of Rolling Friction	0.01
Coefficient of Static Friction	0.8
Coefficient of Restitution	0.5
Surface Energy [J/m ²]	0.001

5. Vibration Powder Dispensing Mass Flow Rate

The goals stated in Section 2.8.1 for a vibration powder dispensing system are:

- A mean flow rate range of 1 – 5 g/min of 316L stainless steel powder.
- Monotonically varying performance by changing one parameter.
- Equal or smaller flow rate variance when compared to the existing industrial system.

5.1. Experimental Setup

The constructed system consists of a 3ml plastic syringe with a stainless steel dispensing tip mounted to a vibration actuator (PI P840.2 piezo actuator, PI E610.0 piezo amplifier) as shown in Figure 14. Dispensing tip diameters used include 680, 861 and 1038 μm . The amount of powder loaded into the syringe was held constant at 10 ± 0.2 g. Once the system was set up and powder was loaded, vibration was turned on for 60 s while measurements of total dispensed mass (using H&C Veritas M314Ai balance) and vibration acceleration (using Freescale FXLN8362Q accelerometer) were taken.

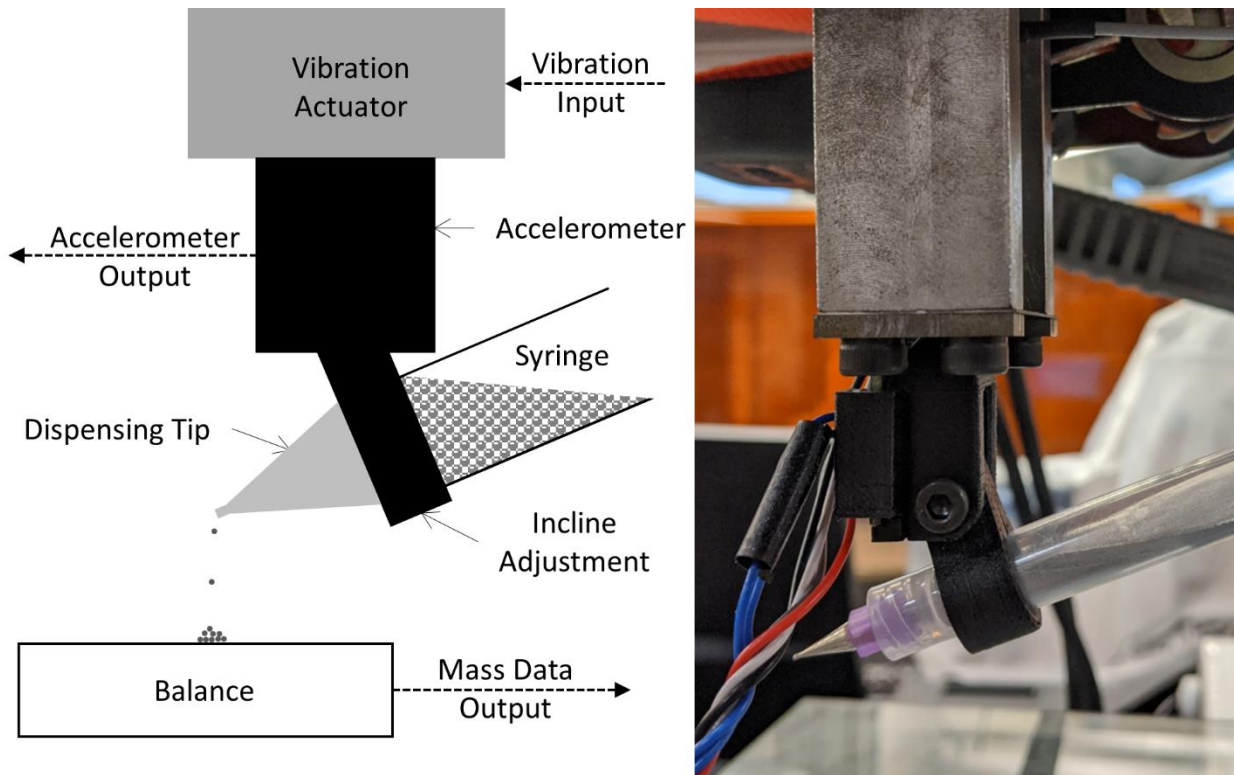


Figure 14: Experimental VPD Setup

Mass flow rate was calculated by performing linear regression on the cumulative mass versus time measurements. The slope of the fitted line is the best-fit mass flow rate and the R^2 statistic can be used to gauge the consistency of the mass flow rate. Peak-to-peak acceleration values were calculated as the difference between the largest and smallest values in each acceleration measurement. The frequency of the vibrations was verified using a fast Fourier transform.

5.2. Simulation Setup

The simulation setup consisted of a tube with a tapered end modeled to match the dispensing tips in the experiments as seen in Figure 15. No geometry scaling was implemented as the particle size and outlet size aspect ratio is an important part of this study. The simulation events are as follows:

- The tube is loaded with approximately 100,000 particles.
- Vibration is applied to the tube and powder begins dispensing.
- A constant number of particles (100,000) is maintained in the tube with a custom particle factory.
- The rate at which particles leave the simulation domain is used to calculate the mass flow rate.

Simulations were run for 2 seconds, long enough to achieve a steady state for all conditions.

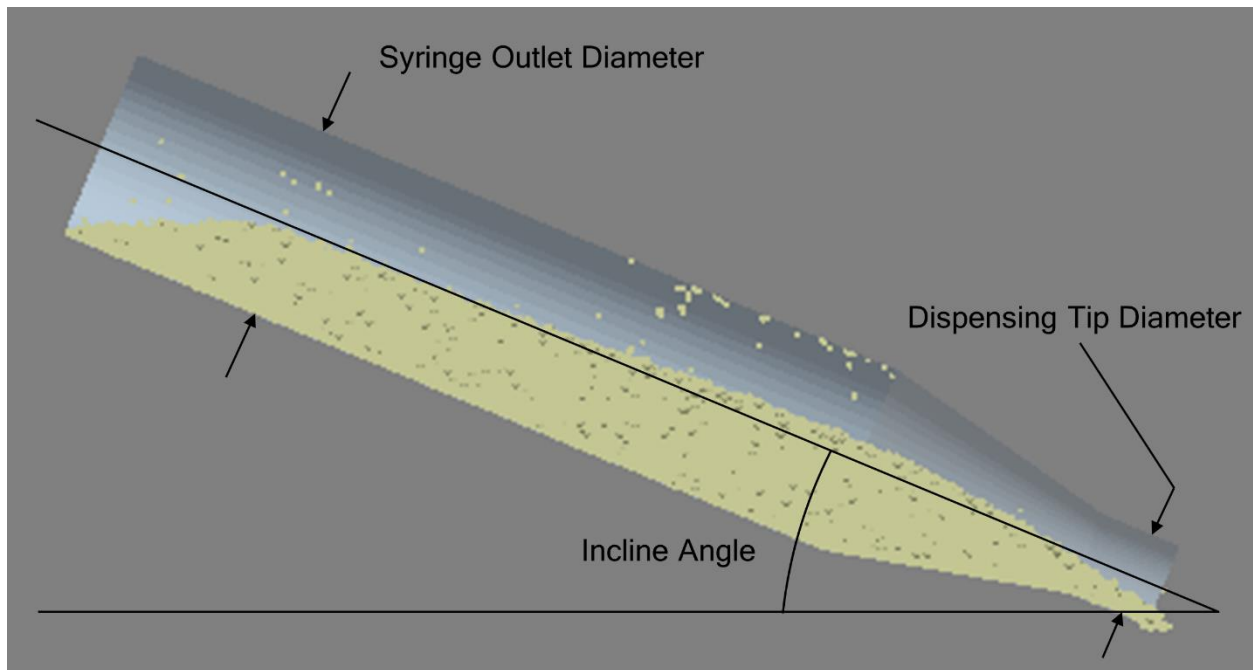


Figure 15: VPD Simulation Setup

5.3. Results and Discussion

5.3.1. Initial Experiment

An initial experiment screened ranges of peak-to-peak vibration acceleration ($10 - 100 \text{ m/s}^2$), vibration frequency ($100 - 1000 \text{ Hz}$) and nozzle diameter ($660 - 1346 \text{ }\mu\text{m}$ straight and $335 - 437 \text{ }\mu\text{m}$ tapered). With the powder used in this study, the vertical nozzle orientation used led to all-or-nothing flow behavior where no varied parameter gave sufficient control over the output mass flow rate.

5.3.2. Screening Experiment

Seeing the failure to achieve control using vertically-oriented nozzles, nozzle inclination was added as a parameter to study, and a screening experiment was created. A $2 * 2 * 3 * 2$ full factorial study with no replicates was conducted with factors and levels listed in Table 13. The results are shown in an ANOVA main effects plot in Figure 16. Nozzle incline has the largest effect and would be simple to continuously control in a machine design. Nozzle diameter also has a significant effect, but is not simple to continuously control in a machine design. Vibration acceleration and frequency, at least in the ranges studied, did not have a significant effect on output mass flow rate.

Table 13: Factors and Levels for Screening VPD Experiment

	Vibration Acceleration [m/s^2]	Vibration Frequency [Hz]	Incline [$^\circ$]	Diameter [μm]
Level 1	31.6	316	22.5	680
Level 2	100	1000	32.5	1038
Level 3	-	-	42.5	-

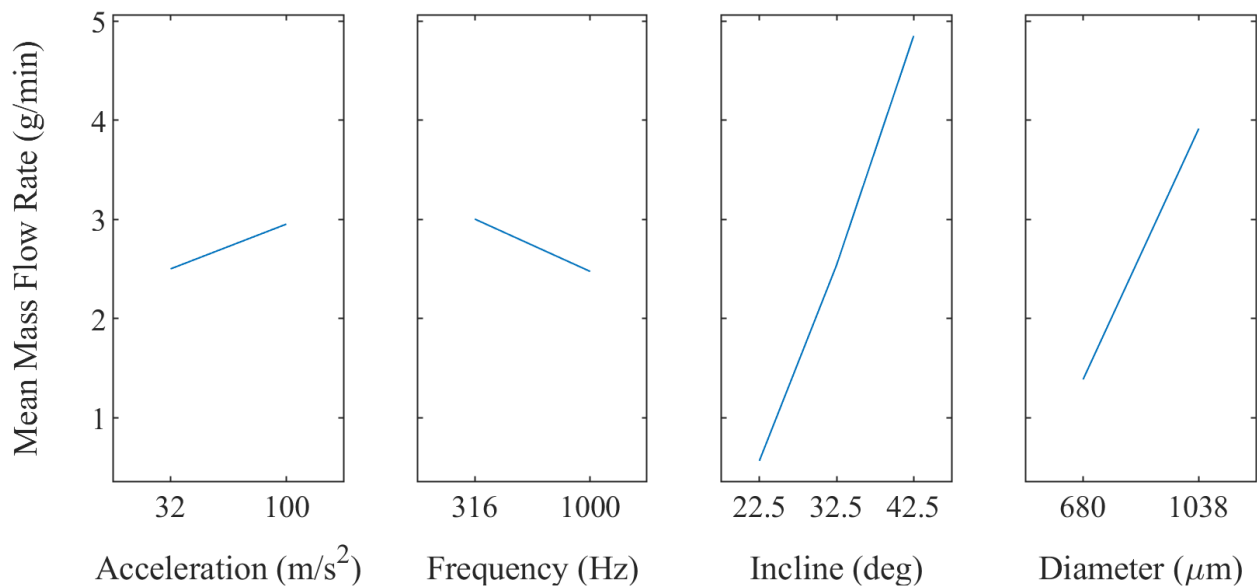


Figure 16: Main Effects for Screening VPD Experiment

5.3.3. Detailed Experiment

Seeing that nozzle inclination and diameter were the two most significant predictors of mass flow rate, a detailed experiment studying those factors and the repeatability over time was created. The factors and levels of the $5 * 3$ full factorial design are shown in Table 14, and six replicates were run for each condition.

Table 14: Factors and Levels for Detailed VPD Experiment

	Incline [°]	Diameter [μm]
Level 1	22.5	680
Level 2	27.5	861
Level 3	32.5	1038
Level 4	37.5	-
Level 5	42.5	-

The results are shown in Figure 17. Evidently the goals of a flow rate range of 1 – 5 g/min and monotonic variation with one parameter can both be achieved by varying nozzle incline with an appropriate nozzle diameter.

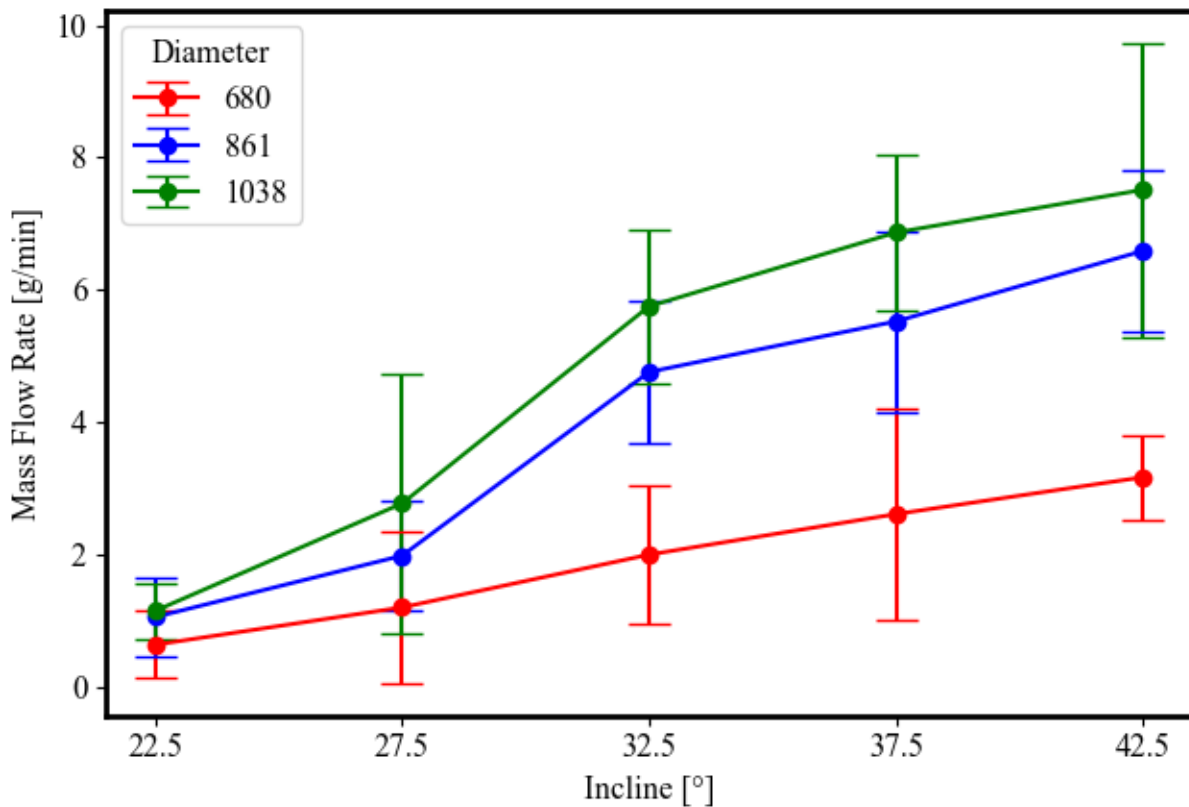


Figure 17: Detailed VPD Experimental Results

The goal of minimal variation in time is more complicated to discern. The 95% confidence error bars in Figure 17 represent a large variance in mass flow rate, but it is important to consider the timeframe of the variance. These error bars show the variation between mass flow rate trials run hours or days apart, while the variation on the time scale of seconds and minutes is small and comparable to that of the existing AMBIT system. The variance between runs is discussed in Section 5.3.5. Because the flow rate changes over longer time

scales and between loadings, it may be possible to implement calibration or feedback control systems to maintain appropriate flow.

For each set of mass flow data collected over 1 minute, linear regression was performed to find the mass flow rate and the resulting R^2 statistic is characteristic from the variance in the mass flow rate. In the majority of VPD samples, R^2 exceeded 0.999, with several between 0.99 and 0.999. The data from the existing AMBIT system showed values also around 0.999. The variance of both systems on the timescale of one minute is comparable and low, and the goal of minimizing mass flow rate variation is met.

5.3.4. Simulation Results

A comparison of the simulation results and experimental results is shown in Figure 18. Agreement is generally good in the ranges studied except for high-diameter, high-incline experiments. The variability discussed in Sections 5.3.3 and 5.3.5 does not account for this discrepancy. Further refinement and calibration was deemed unnecessary as no analysis or outcomes would be based on these results.

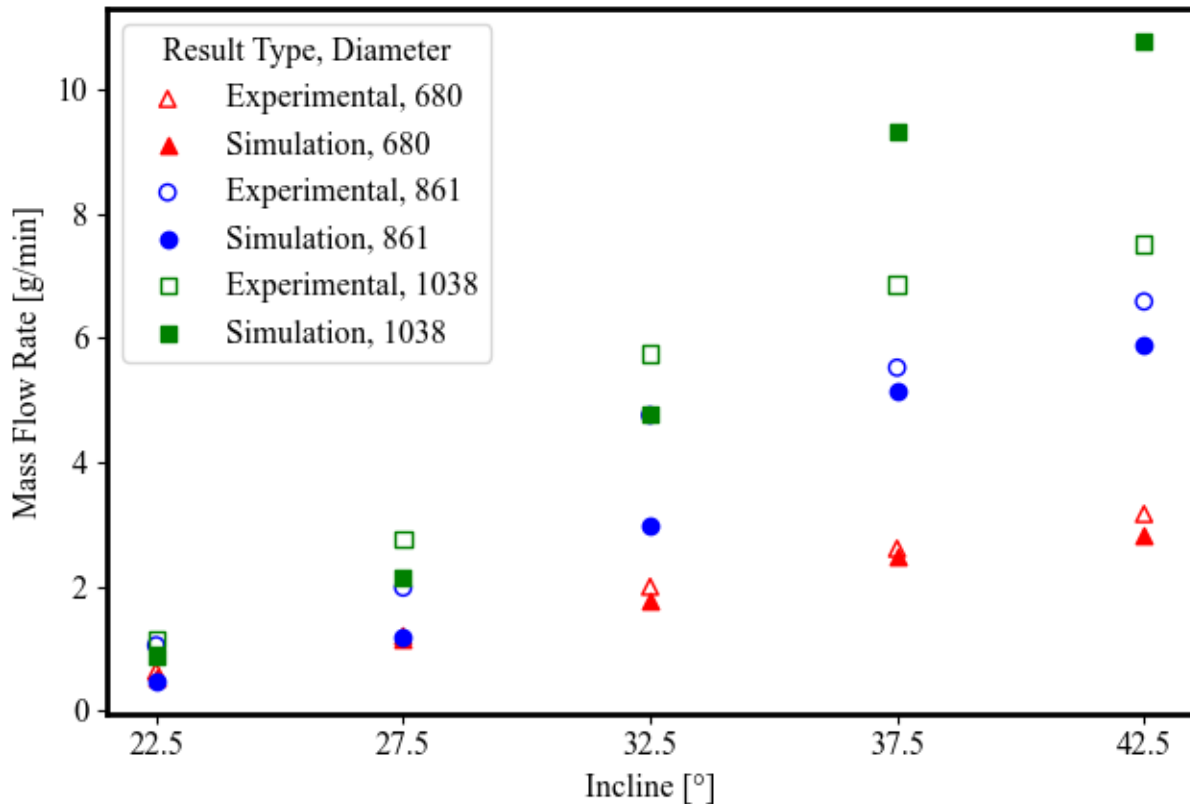


Figure 18: Simulation and Experimental VPD Result Comparison

Simulation results revealed some details about the mechanics of the VPD process that would be difficult to observe and measure using experimental methods. Figure 19 shows the particles in the midplane of the dispensing tip and the magnitude of their velocities. The image shows there is a portion of powder at the outlet with higher than bulk velocity,

shown in green-red colors. The number of particles in this faster-moving region, as well as the speed at which they move, both increase with incline.

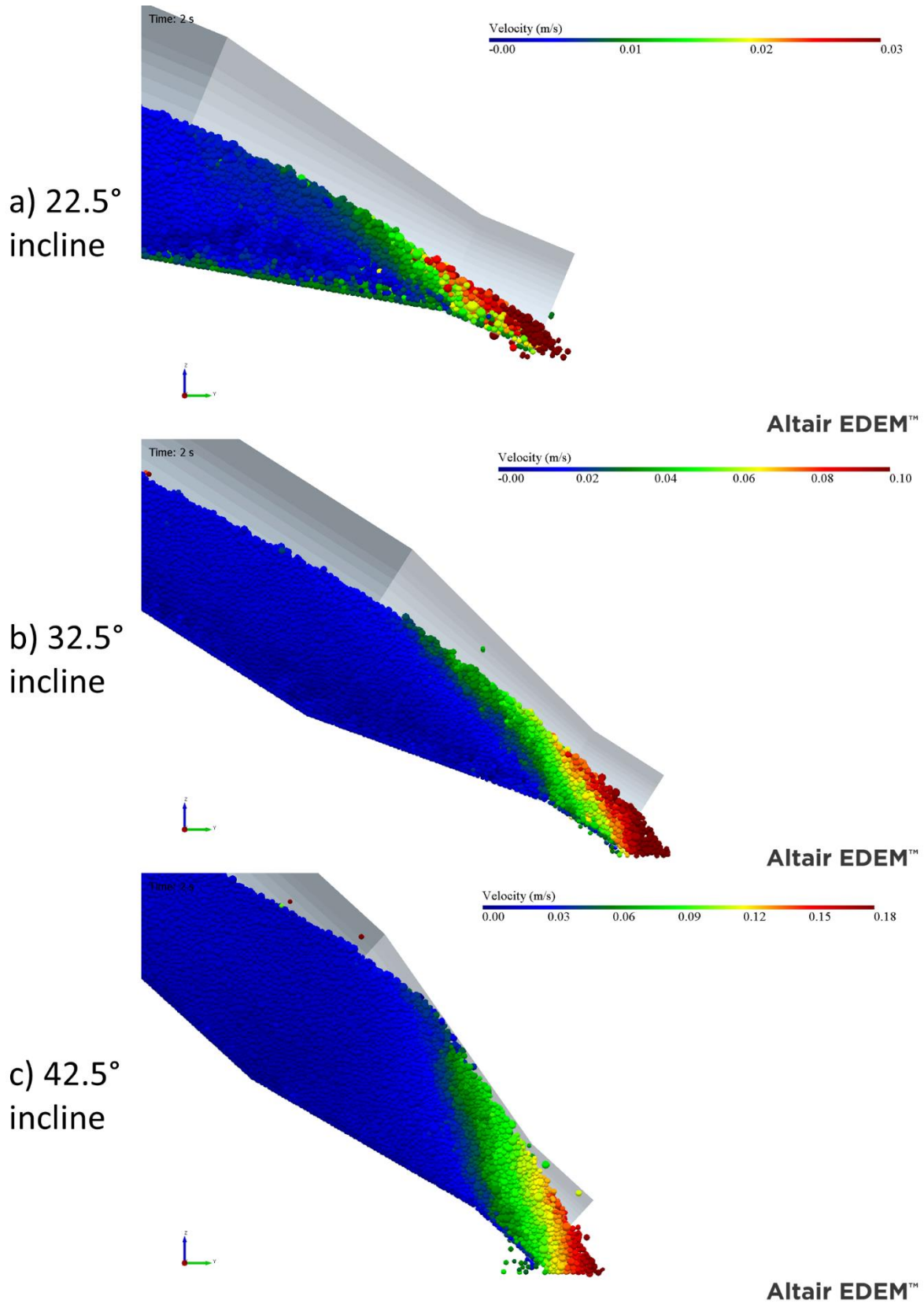


Figure 19: VPD Simulation Incline Comparison (Diameter=1038 μm)

5.3.5. Additional Work with Powder Flow Variability

One significant source of flow rate variability lies in the loading of powder into the system. Six powder flow rate measurements were taken successively over the span of several minutes where no other factor could have changed significantly and the system configuration was not altered. Though the scoop spatula used to guide the powder into the syringe was held parallel to the syringe and the powder was poured at a similar rate, there was certainly some variation that occurred during this human-driven process. Looking at the flow rate results of the six runs, the overall flow rate mean is 6.11 g/min with a standard deviation of 0.76 g/min, in line with previous experimental results. However, if the two low-flow outliers are omitted, the mean flow rate becomes 6.60 g/min with a standard deviation of 0.04 g/min. These results suggest that loading variability could easily account for the high variability in the VPD mass flow rate results, and also that future work into finding the cause of low-flow outliers could yield very low variability for the mass flow rate across all time scales.

While not as important as loading variability, environmental conditions can create variability in powder flow. To understand the contribution of environmental effects, specifically humidity, on the powder flow rate during VPD, powder flowability experiments in a controlled atmosphere were conducted. Hall flow tests following ASTM B213-17 [30] were run in a glovebox first purged with nitrogen to achieve a dry state. Subsequently, small amounts of water were boiled to achieve increasing levels of humidity. To help ensure accuracy, the measurements were taken a few minutes after the hygrometer reading stabilized.

In the range of humidity that the air-conditioned lab typically has (typically around 50% and almost always between 25-75%), there is a small but significant difference in powder flowability. As shown in Figure 20 below, there is about a 3% difference in flowability observed between relative humidity levels of 26.1% and 58.4%. The variability observed in flow rates in VPD experiments is significantly higher than this, suggesting that the uncontrolled environment during those tests was not the main source of variability.

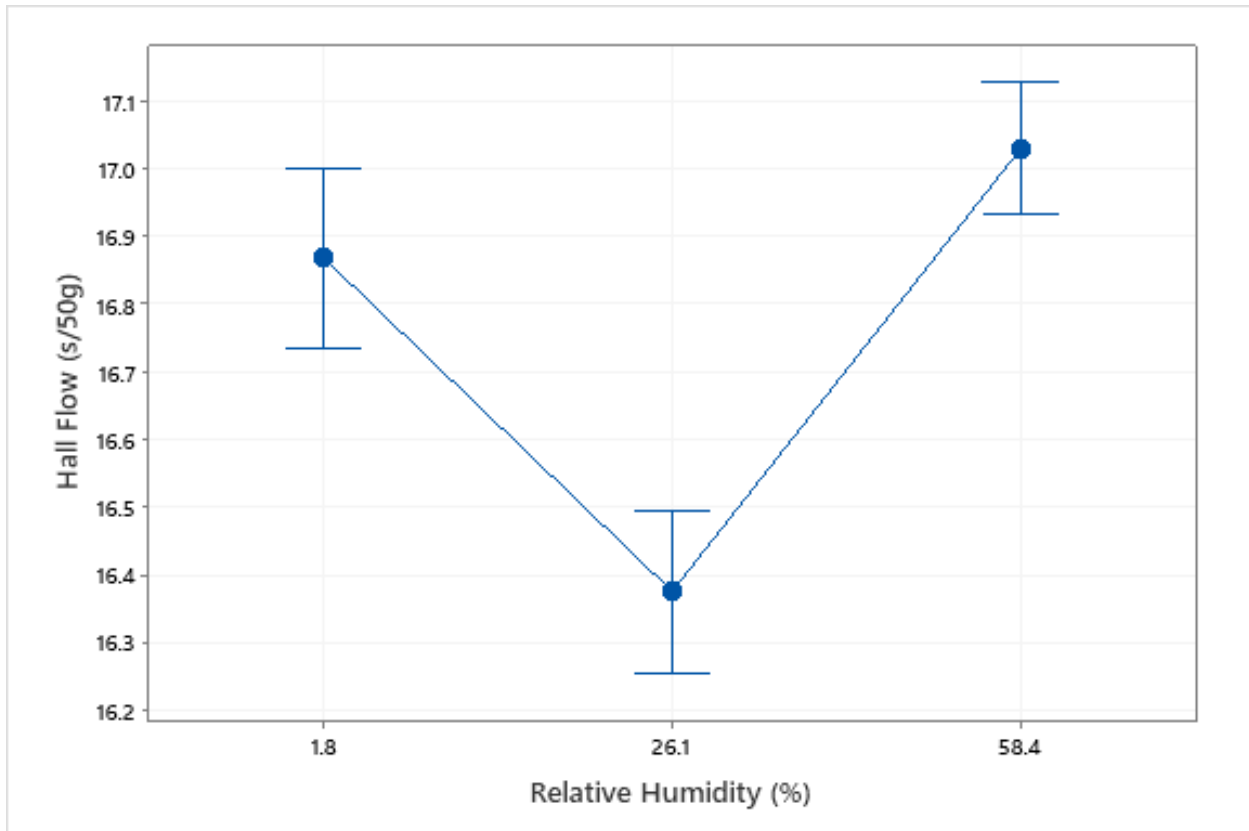


Figure 20: Hall Flow of Powder at Different Humidity Levels

Looking at the extreme ranges of humidity, very dry conditions show a similar level of flowability to the normal conditions. Interestingly, the very dry condition (1.6% RH) flowed slightly slower than the somewhat dry condition (26.1% RH). This behavior could be useful to understand if operating a VPD system in an inert atmosphere. A very high level of humidity (89.1% RH) was also measured, but at this point the powder did not flow in the funnel and no data is reported. This is well understood in industry and machines that work with powder are typically installed in climate-controlled areas.

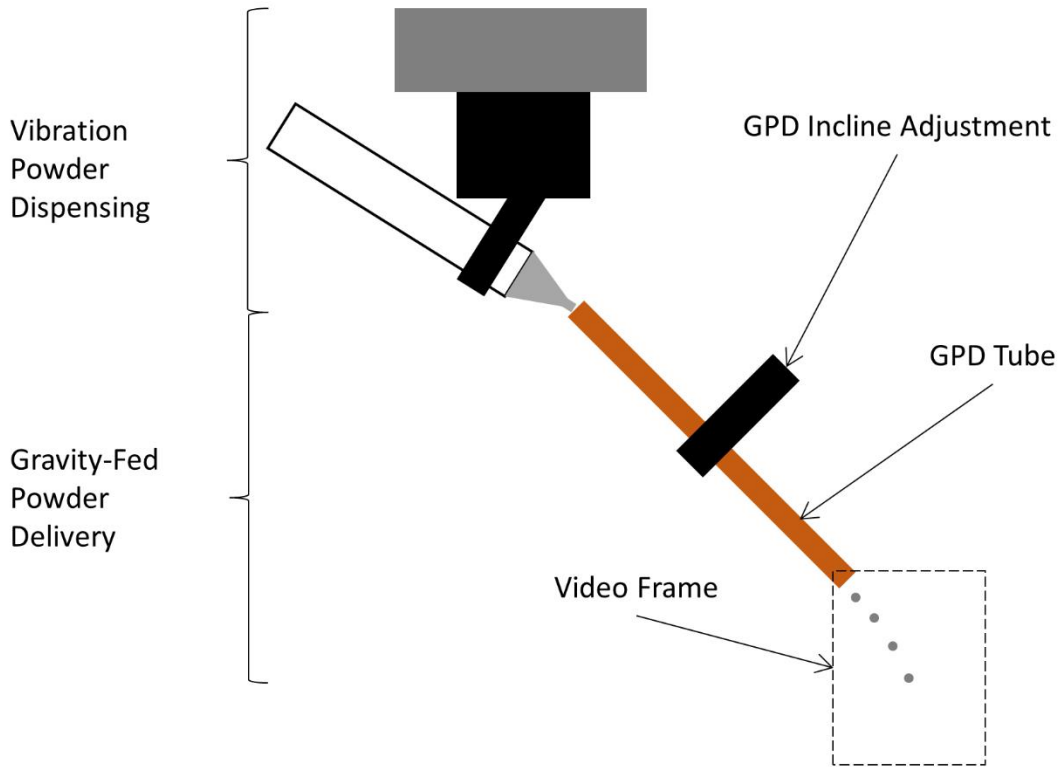
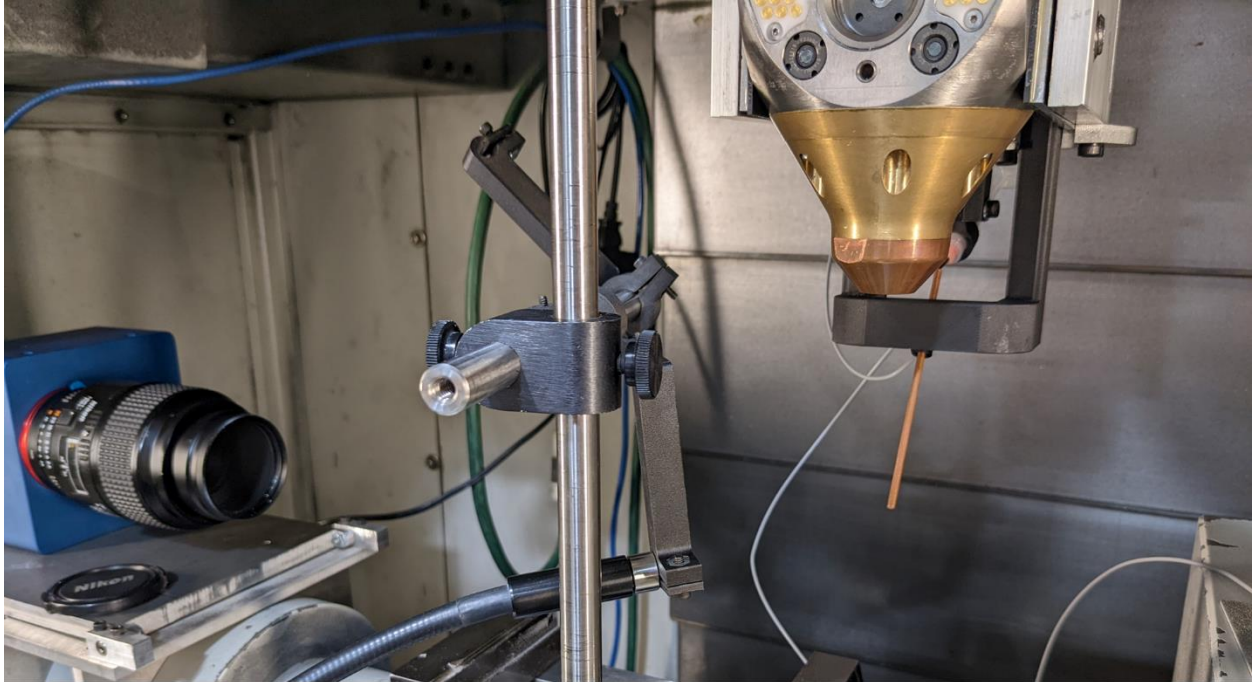
6. Gravity-Fed Powder Delivery Stream

Gravity-fed powder delivery propels powder in a controlled fashion toward a target area by using only inclined solid material and gravity. The goal for this subsystem as set out in Section 2.8 is to achieve a high powder capture efficiency. However, that must be measured at a system level and the goal during subsystem testing will be reducing the size of the powder stream below the size of the system's laser beam.

6.1. Experimental Setup

The goal of this experiment is to quantify 1) how the powder stream disperses in space after leaving the delivery tube and 2) the velocity with which it leaves the tube. High-speed camera footage can be processed to measure both. By binarizing the pixels of each frame (particle = 1, no particle = 0) and overlaying all the frames, a 2D probability distribution of particle location is created. One caveat in this technique is that in a 2D frame, it is possible for one particle to obscure another particle and that pixel, when binarized, will only count for one unit in the probability distribution. However, as the chances of this happening are higher in the high particle density section in the center of the stream, the unaccounted-for mass is expected to be in the center of the stream, which will make the measurements a conservative underestimate of the mass distribution.

The setup consisted of the video camera, the vibration powder dispensing system and the gravity-fed powder delivery system. The VPD system was not modified from the earlier experiments but was mounted into a system that also contained the GPD system. A diagram and photograph of the system are shown in Figure 21.



(Camera's Perspective)

Figure 21: GPD Experimental Setup

The GPD system is very simple. A copper tube with a 3mm outer diameter, specified length and specified inner diameter is mounted in a bracket that allows its incline to be set. The entire system can move vertically to allow alignment with the VPD system as necessary.

Four parameters were varied for this experimental study: tube length, tube incline, tube inside diameter and VPD syringe incline (which is correlated with mass flow rate). The factors and levels are shown in Table 15 below. Two total replicates of the 2⁴ full factorial study were measured.

Table 15: GPD Experiment Factors and Levels

Factor	Tube Incline (°)	Tube Length (mm)	Tube Diameter (µm)	Syringe Incline (°)
Level 1	45	50	600	22.5
Level 2	55	100	1000	32.5

To perform an experimental run, the following procedure was used:

- Set syringe incline and dispensing tip diameter
- Install tube with appropriate length and diameter
- Set tube incline and align to dispensing tip
- Load 10 g of powder into syringe
- Move to video position and ensure position and focus
- Turn on vibration and begin powder dispensing
- Trigger high-speed video and save

Each video was processed as described before into a probability distribution, then two values were extracted from the distribution. First, the radius containing 95% of the mass at a height 10 mm below the tube exit was found. Second, the exit velocity was calculated using freefall kinematics and the distance travelled orthogonal to gravity at a given height of the distribution mean.

6.2. Simulation Setup

The DEM simulations of the GPD process involved just the delivery tube and not powder dispensing. An example geometry with powder flowing through and out of it is shown in Figure 22. As a substitute for simulating the powder dispensing, powder was created at the same rate that previous VPD simulations predicted for the desired conditions.

The factors and levels used in the experimental work were duplicated in simulations, with the addition of exploring the tube material coefficient of static friction and coefficient of restitution. This resulted in a 2⁶ full factorial study. The goal of studying the material properties was to determine their relative effect on performance and if higher or lower levels were advantageous. The factors and levels used are shown in Table 16.

Table 16: GPD Simulation Factors and Levels

Factor	Tube Incline (°)	Tube Length (mm)	Tube Diameter (μm)	Mass Flow Rate (g/min)	Coefficient of Static Friction	Coefficient of Restitution
Level 1	45	50	600	1.05	0.3	0.2
Level 2	55	100	1000	4.75	0.8	0.8

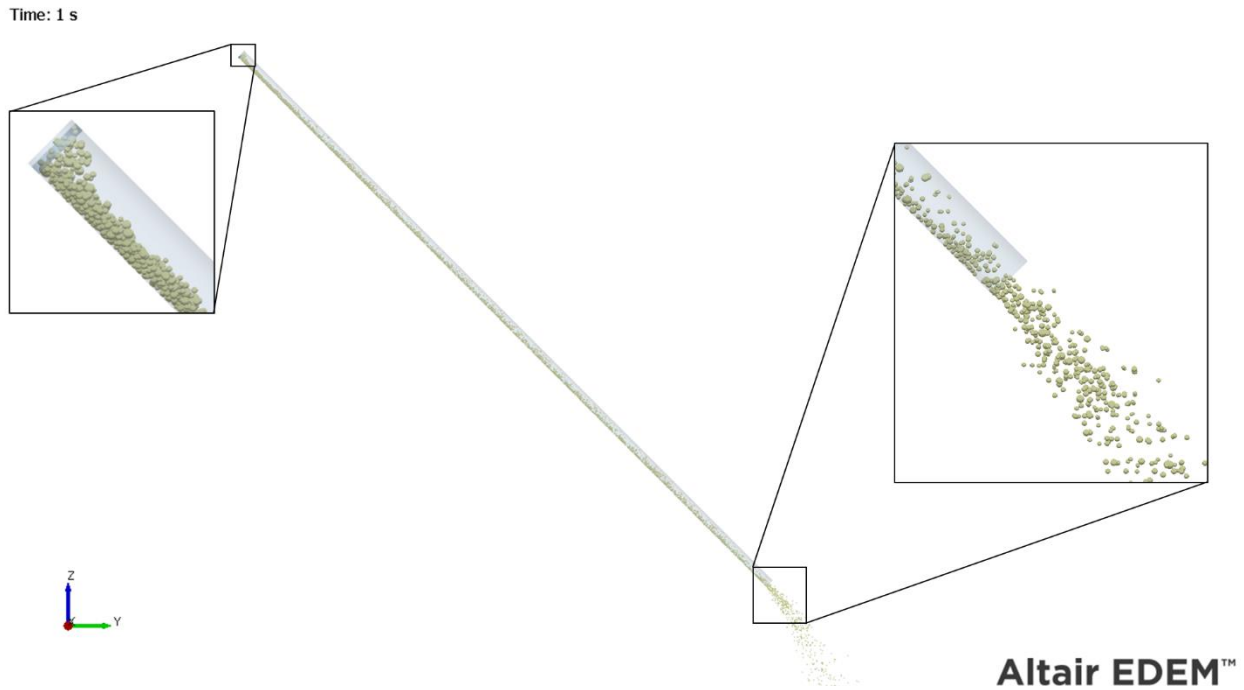


Figure 22: GPD Simulation Setup

6.3. Results and Discussion

6.3.1. Experimental Results

The measurements extracted from the high-speed video data were run through standard Design of Experiments analysis using Minitab. Separate analysis was conducted for spread and velocity, both of which found no significant interaction effects at the 95% confidence level.

Looking at spread, the two significant effects are the tube diameter and the syringe incline (which correlates positively with mass flow rate). The tube incline and length were insignificant. The main effects plot is shown in Figure 23. Tube diameter has the largest effect, with smaller tube diameters reducing the spread. This can most likely be attributed to a smaller diameter tube reducing a particle's ability to move in directions orthogonal to the tube axis.

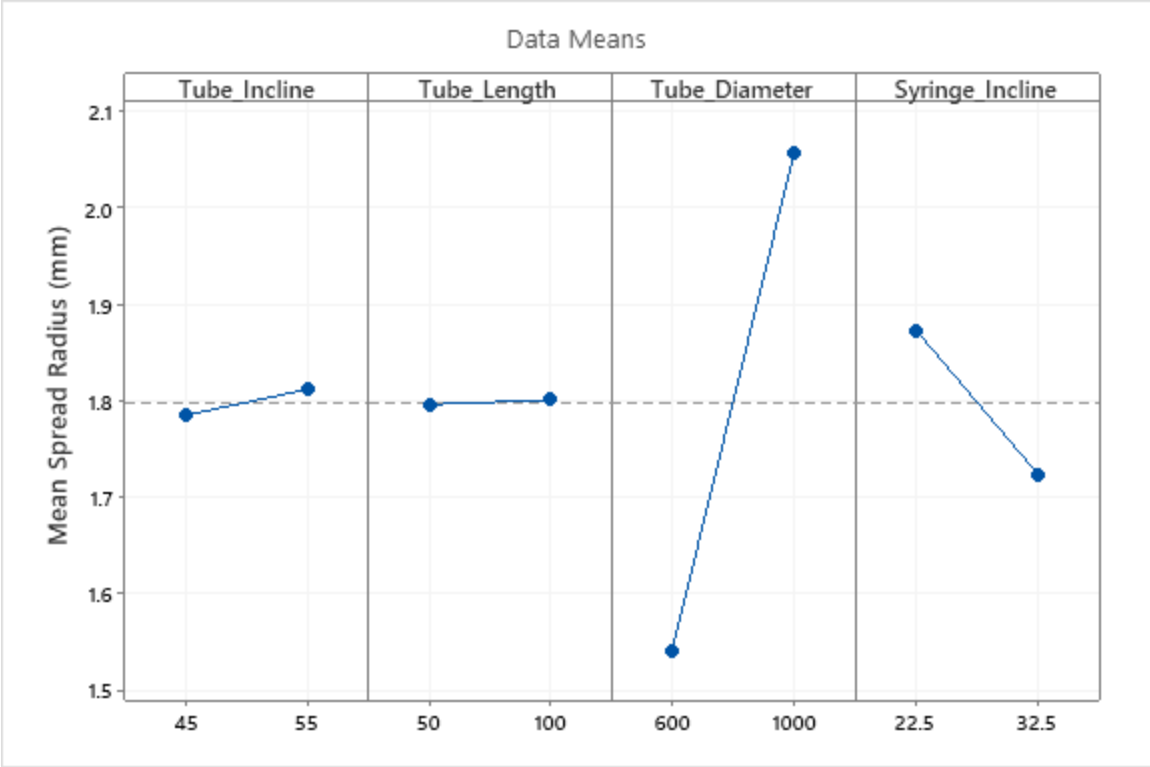


Figure 23: Main Effects for GPD Experimental Spread

Looking at velocity, the two significant effects are tube incline and tube diameter. Tube length was not significant, but it is important to note that that conclusion is only true for the lengths studied in this experiment. The main effects plot is shown in Figure 24.

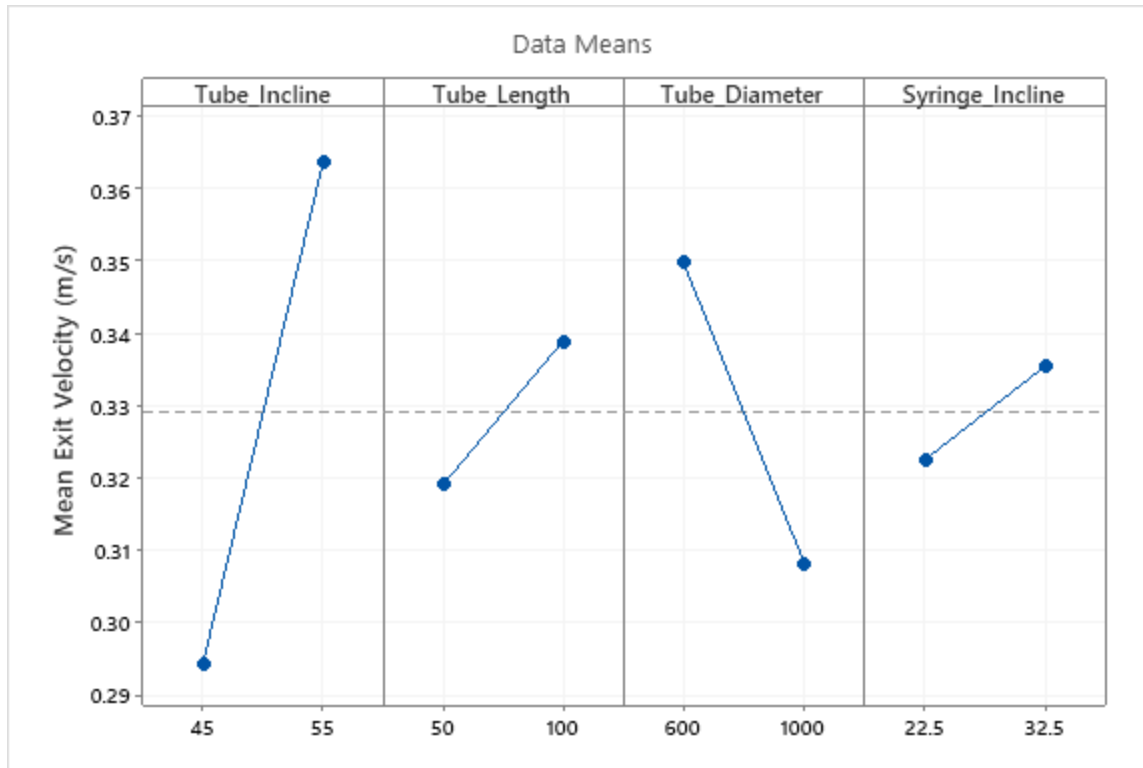


Figure 24: Main Effects for GPD Experimental Exit Velocity

6.3.2. Simulation Results

The main effects plot for particle spread radius in the 2^6 full factorial simulation study is shown in Figure 25. All effects except tube length are significant. The tube coefficient of static friction and coefficient of restitution are the two most significant effects and the interaction between them is also significant.

To better understand how the two tube material properties affect the spread, it is useful to divide the full 2^6 study into four 2^4 full factorial studies, one for each of the combinations of tube material properties, as well as looking at the ANOVA interaction plot. Figure 26 and Figure 27 show that the combination of low static friction (0.3) and high restitution (0.8) dramatically reduces the mean spread radius compared with all other combinations, which are all fairly similar.

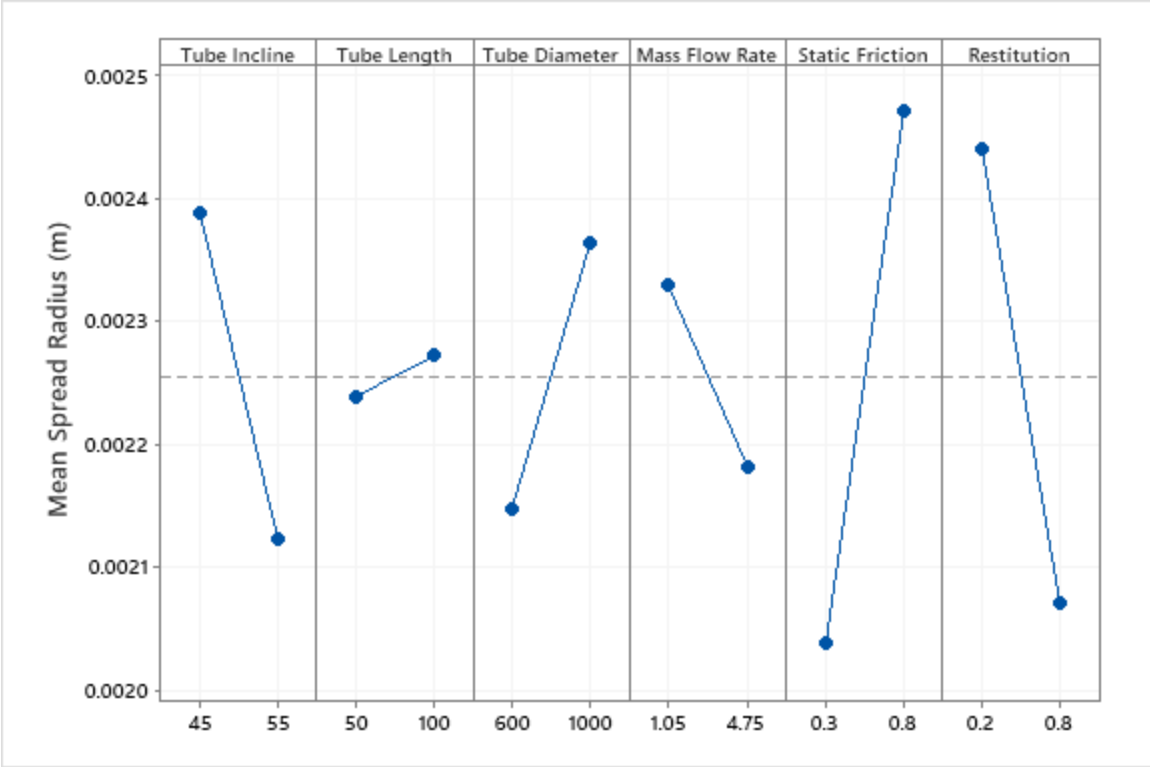


Figure 25: Main Effects Plot for Spread in GPD Simulations

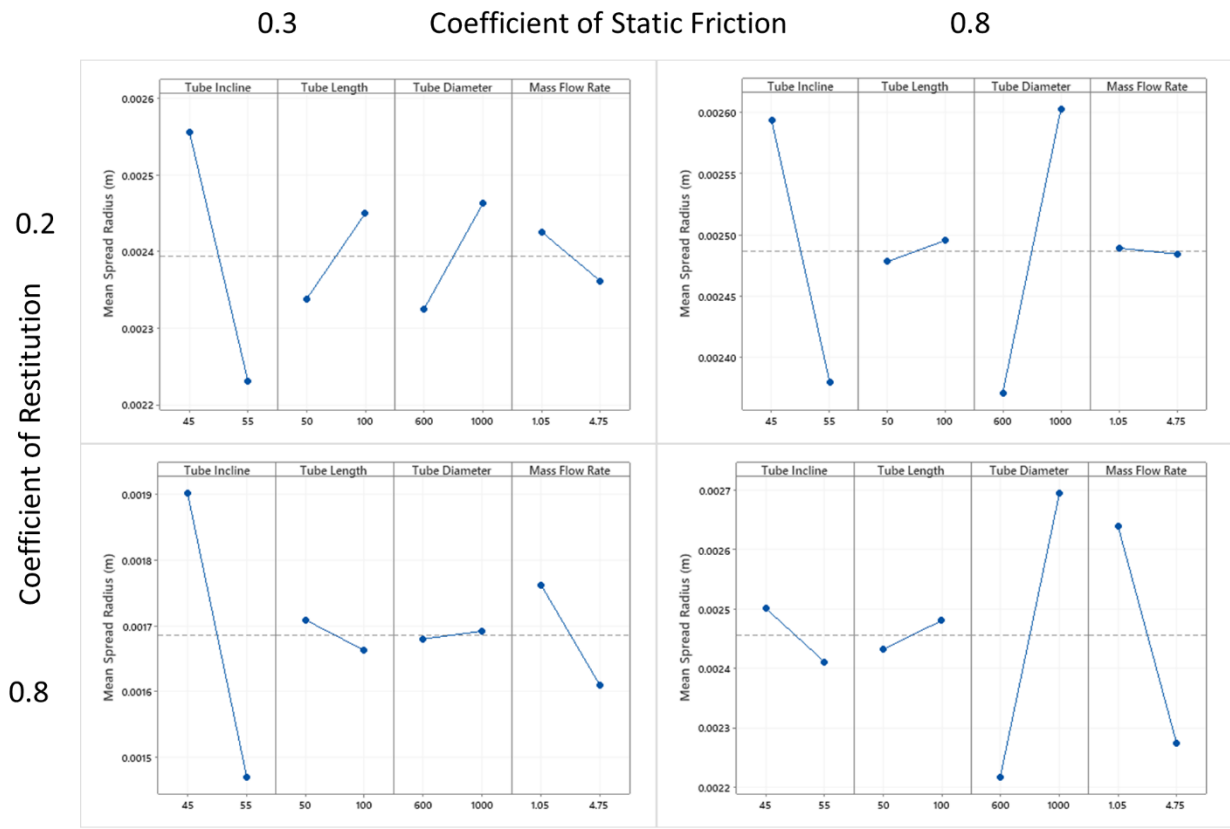


Figure 26: GPD Simulation Spread Main Effects Plots Divided

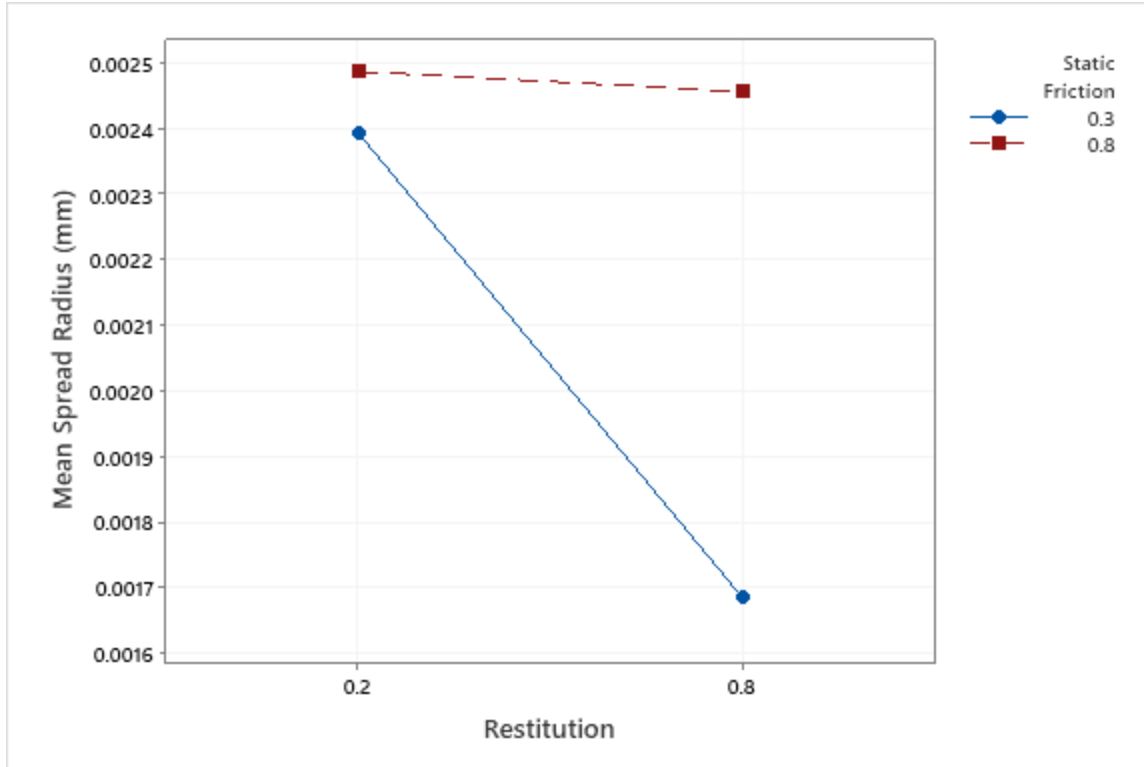


Figure 27: GPD Simulation Spread Interaction Plot

The main effects plot for mean particle exit velocity is shown in Figure 28. Here, all factors are significant as well as the interaction between coefficient of static friction and coefficient of restitution. To make the data easier to understand, four plots detailing the main effects for each combination of material properties are shown in Figure 29 and the interaction plot for static friction and restitution is shown in Figure 30.

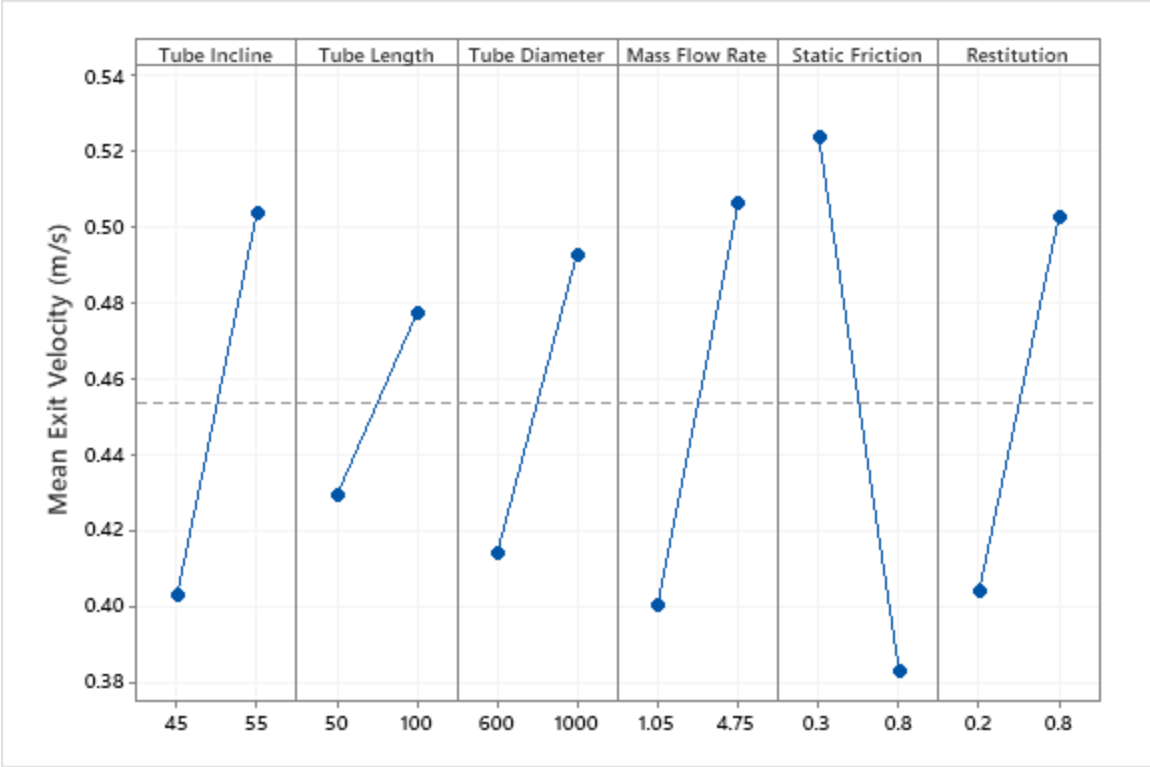


Figure 28: Main Effects Plot for Velocity in GPD Simulations

0.3

Coefficient of Static Friction

0.8

0.2

Coefficient of Restitution

0.8

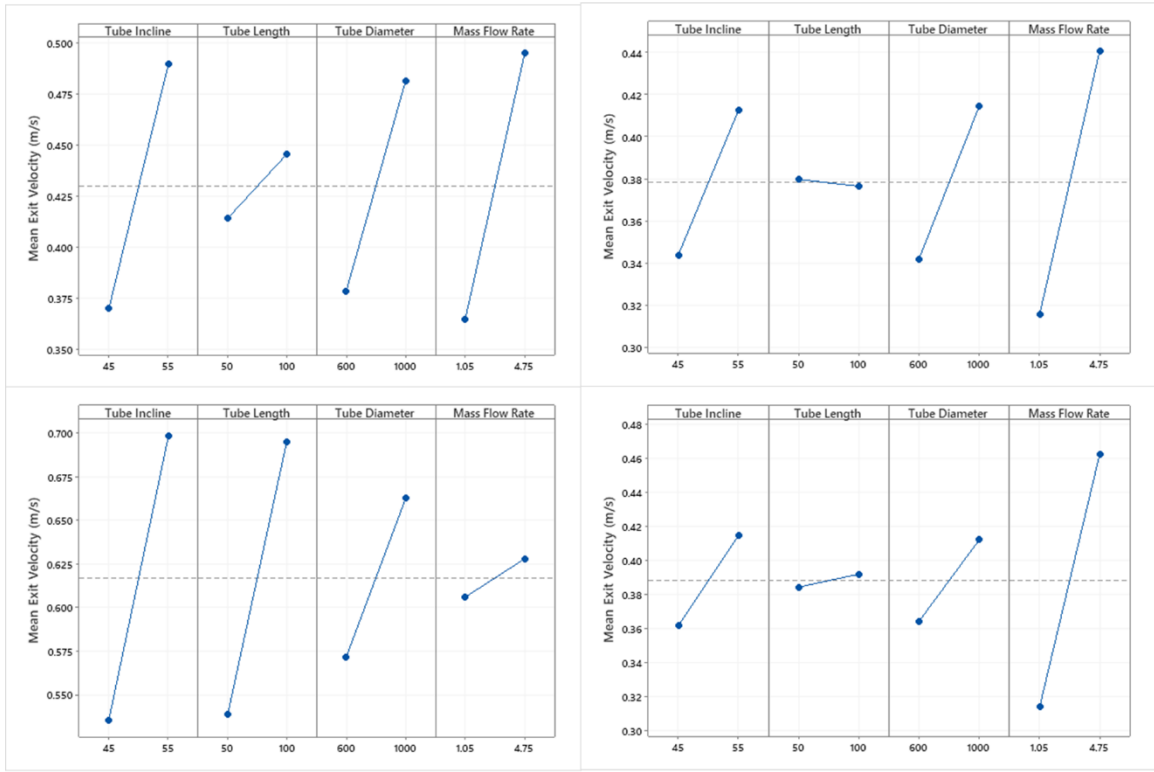


Figure 29: GPD Simulation Velocity Main Effects Plots Divided

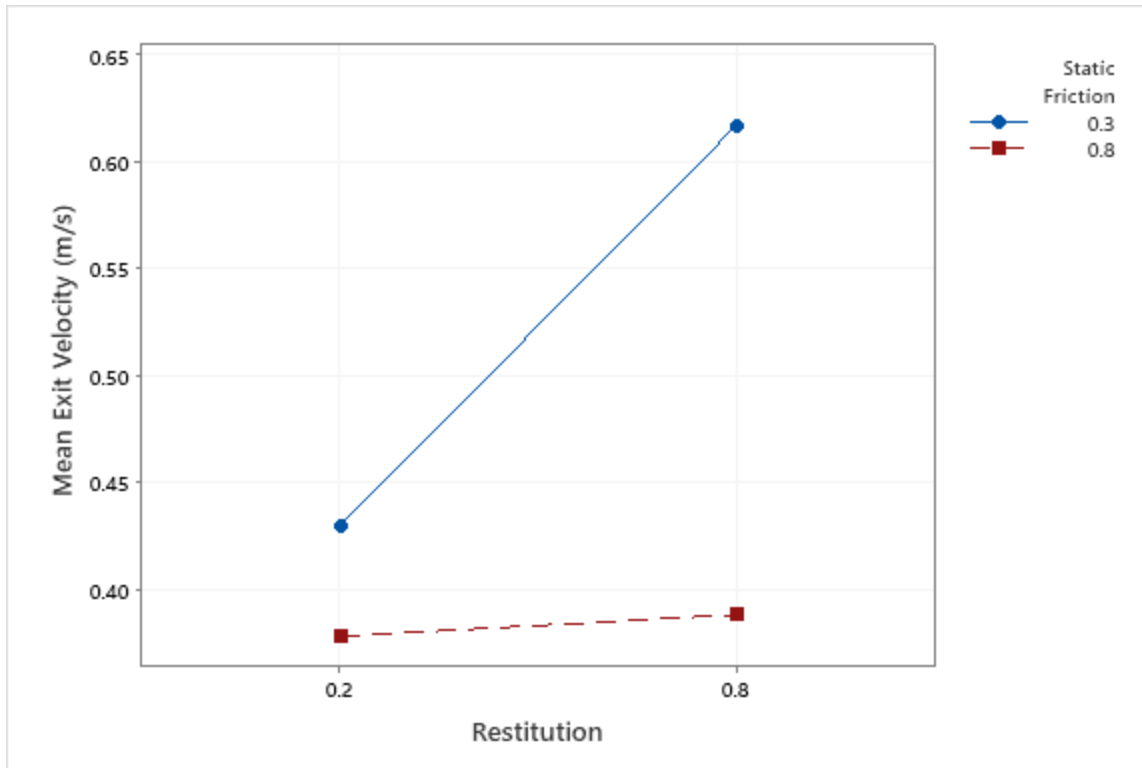


Figure 30: GPD Simulation Velocity Interaction Plot

As with the spread results, the combination of low coefficient of static friction and high coefficient of restitution is significantly different from the others, which are all similar in comparison.

6.3.3. Discussion

It is understandable that the combination of low friction and high restitution leads to high exit velocity, as both high friction and low restitution serve to reduce particle velocity when a collision with the tube wall occurs. Understanding why low friction and high restitution create low spread is more challenging. Figure 31 shows that across all conditions in the full 2^6 simulation study, there is an apparent correlation between spread and velocity. This can be attributed to the different mean velocity and spread values obtained for the high coefficient of restitution and low coefficient of static friction subset of values. Figure 32 shows the velocity and spread values for the four subsets, all of which have weak or no correlation, disproving the notion that velocity by itself reduces spread. Additional work into understanding the parameters that drive the spread of the powder stream will be important for future improvements to this system.

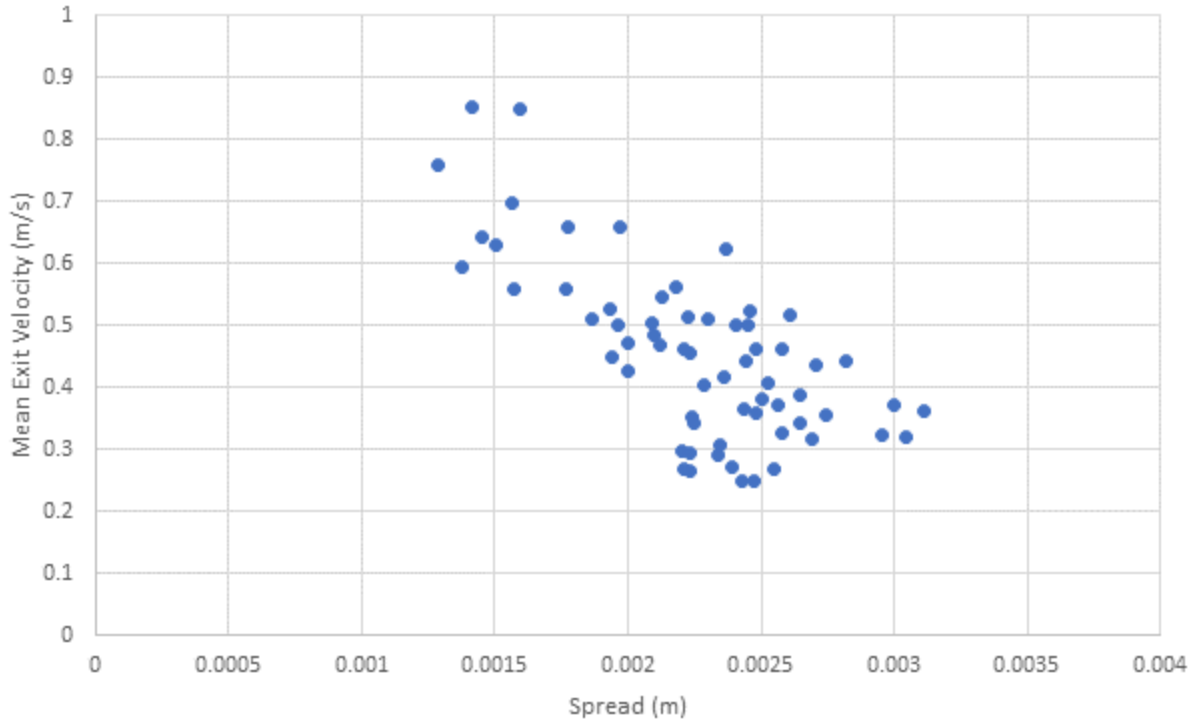


Figure 31: Velocity and Spread Correlation for All Conditions

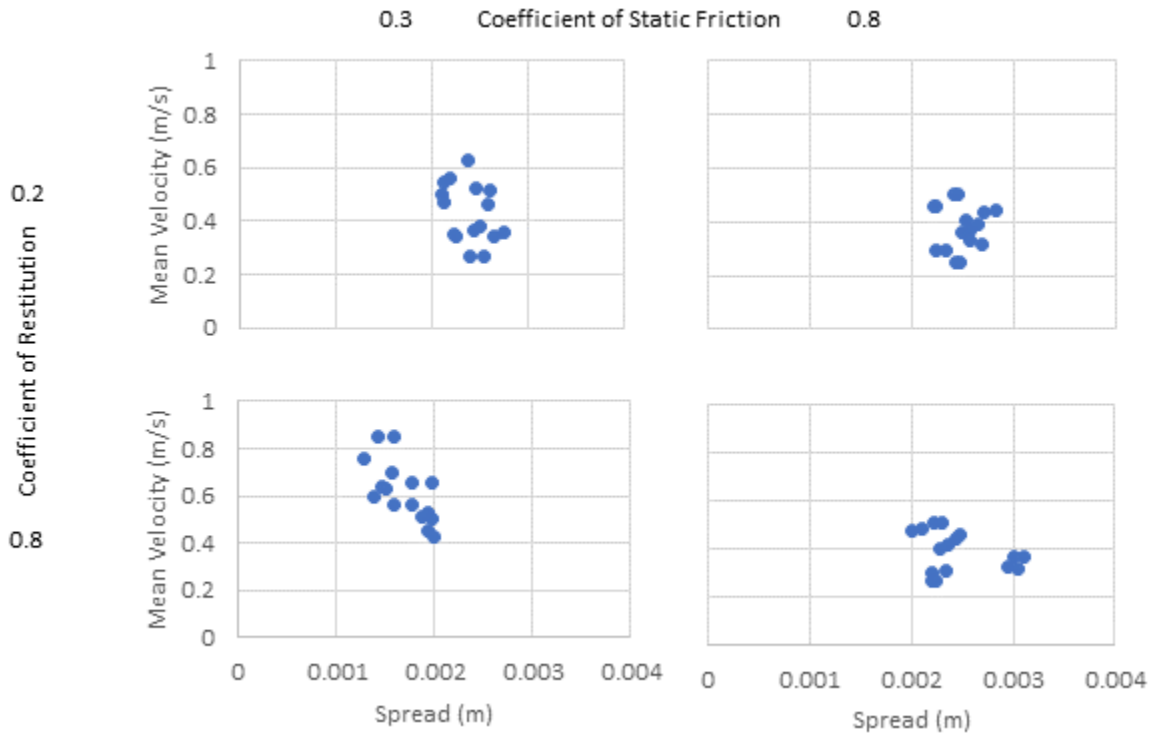


Figure 32: Velocity and Spread for Subsets of Conditions

7. Control Lag

The control lag of the system revolves around the time between the system controller commanding a change and the change taking effect in the process. The goal of studying control lag in this work is not to provide exhaustive proof that the proposed system has lower lag, but to demonstrate that it is an improvement in the most common situations encountered while processing.

The control lag of the proposed system will be measured in one situation, turning on and off with the application of vibration. No other controls are available at this point in development. The control lag of the existing conventional system will be measured in the same way, turning on from a state of no powder flow, as would be the case when printing the first portion of a part. Conventional designs vary greatly and could certainly reduce the control lag, but the measurements taken can be seen as a “normal” or “common” value.

7.1. Experimental Setup

A balance is positioned to collect the powder being dispensed and mass data from it is logged using a computer. The beginning of the data recording and sending of the control command happen simultaneously.

The mass data is then analyzed in terms of mass flow rate. The time when the mass flow rate is deemed stable at the expected value is the control lag.

7.2. Results and Discussion

Mass versus time data is shown in Figure 33. The blue curve shows that the conventional system takes about 16 s to reach a steady flow as commanded. The red curve shows that the proposed system takes only about 3 s, which is significantly faster. It should be noted that the spike in mass at around 2 s in the conventional system curve is powder that stayed in the line from a previous command being dispensed before the steady flow from the powder feeder system reached the outlet.

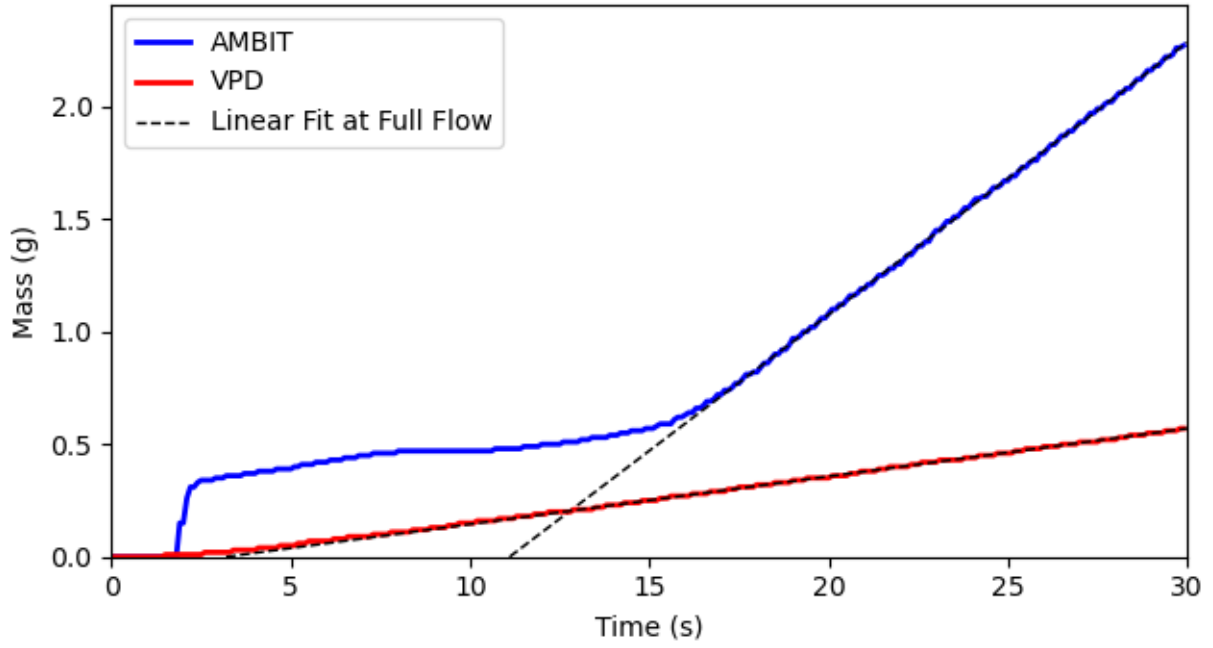


Figure 33: Control Lag Comparison

8. Powder Capture Efficiency

The studies in Chapters 5 and 6 were performed to understand the fundamentals of the vibration powder dispensing and gravity-fed powder delivery subsystems. With this understanding, the goal is to use the new powder delivery system in a realistic directed energy deposition setting and show that it gives excellent powder capture efficiency. Experimental measurements of powder capture efficiency will be taken using the conventional system and the one under study to understand the level of benefit that can be achieved in a real application.

The detailed studies leading up to this experiment give insight into how to control the two main characteristics of the powder stream, the spread and mean velocity. Choosing a spread is very simple as it should be as small as possible to achieve high powder capture efficiency. Selecting the value for the mean velocity is harder because it affects not only the powder capture but also the entire welding process. Mean particle velocities that are too low create a fatal issue in which the particles spend so much time in the laser beam before entering the melt pool that they vaporize. Detailed discussion of the tradeoffs and impacts is provided below.

8.1. Experimental Setup

8.1.1. Equipment

The equipment used in this study is shown in Figure 34. Unlike the GPD experiments, the tube is fixed at one incline and rigidly attached to the tool with the laser, making precise alignment possible. While the design of this system is informed by the results of previous experiments, there is one significant departure. The GPD tube has an inner diameter of 1.0 mm, even though the 0.6 mm diameter showed better powder delivery performance. This choice was necessary because the 0.6mm tube clogged from time to time. The designs used by Wang and Li [2] had the dispensing tubes subject to the powder dispensing vibration, which may have helped prevent clogging.

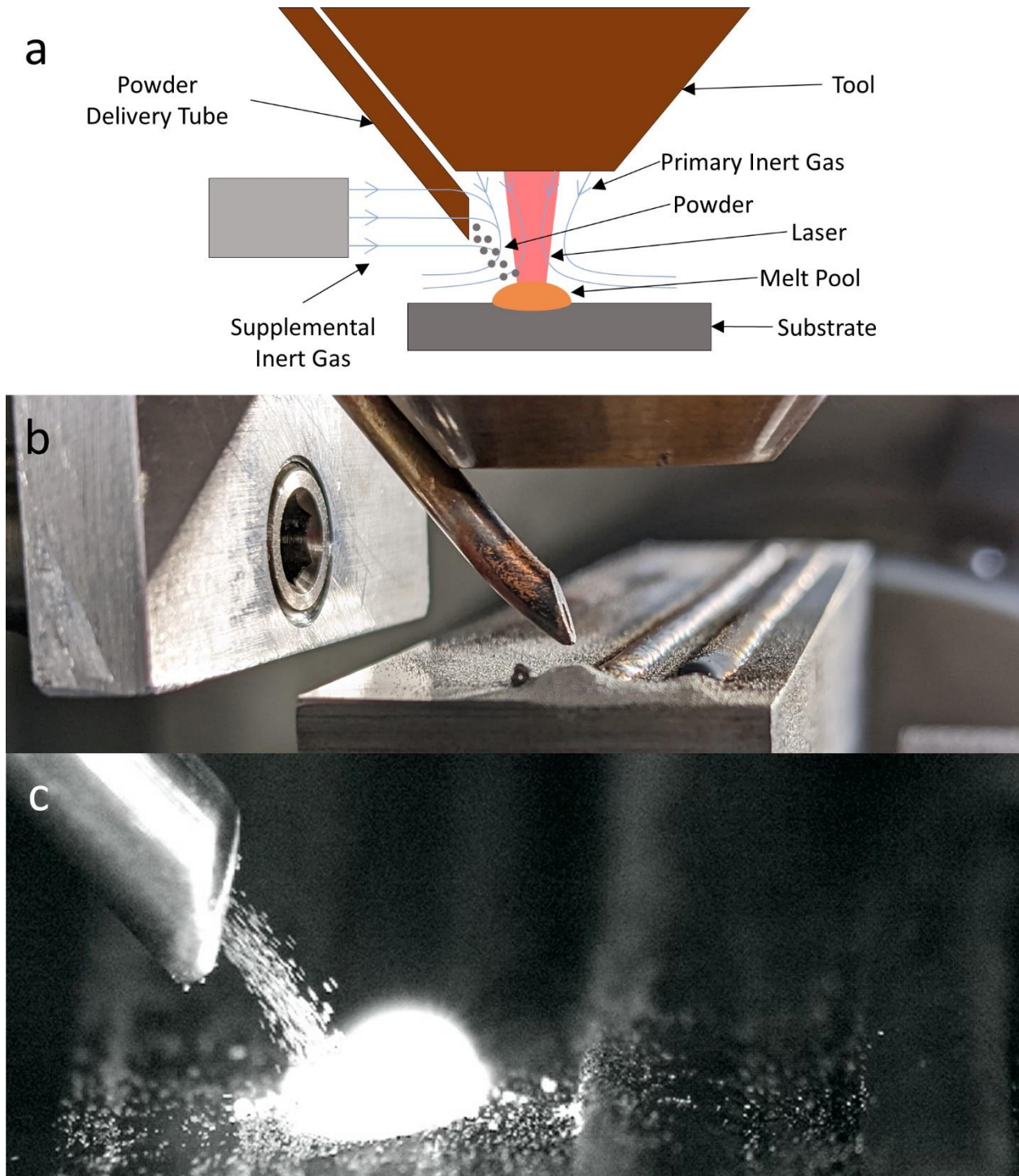


Figure 34: Powder Capture Efficiency Experimental System: a) system components, b) system after printing, c) system during printing

8.1.2. Shielding Gas

While not the focus of this work, having acceptable shielding gas in the welding process is crucial for success. After working through other issues with alignment and parameter selection, there was still a need to improve the shielding gas flow beyond what the conventional tool offered. The approach that gave the best results was to add a supplemental flow with a similar velocity to the shield gas from the conventional tool to the backside of the delivery tube. This configuration was chosen because it was simple to implement and overcame several possible problems. First, it reduced the possibility that air entered the shield gas flow as it goes around the powder delivery tube. Second, the flow was directed from behind the powder toward the laser beam, which increased the horizontal velocity of the powder and allowed a process configuration in which the powder spent less time in the laser beam before entering the melt pool.

8.1.3. Procedure

The steps taken to measure powder capture efficiency are as follows:

- The powder flow rate of the system is measured.
- The mass of the substrate before printing is measured.
- Single tracks of material are printed with known length and feed rate.
- The mass of the substrate with printed single tracks is measured.
- The printed mass, $m_{printed}$, is calculated as the difference in substrate mass before and after printing. The dispensed mass, $m_{dispensed}$, is calculated using the measured mass flow rate, \dot{m} , feed rate, v , and total print track length, l . The ratio of the masses gives the powder capture efficiency, $\eta_{capture}$.

$$m_{dispensed} = \frac{\dot{m}l}{v} \quad (32)$$

$$\eta_{capture} = \frac{m_{printed}}{m_{dispensed}} \quad (33)$$

8.2. Results

The conditions for the VPD and GPD subsystems were chosen based on the results from their respective studies in Chapters 5 and 6 as well as practical experience with the system. The remaining conditions of laser power and feed rate were selected using the mass flow rate and previous data from conventional machine operation. The conditions are provided below in Table 17. The sizes of the outlets for the gas both coaxial and perpendicular to the laser are nearly identical, so setting the flow rate of gas the same through them will give nearly identical gas stream velocities.

Table 17: Powder Capture Efficiency Experiment Conditions

Parameter	Value
VPD Syringe Incline	40°
VPD Vibration	100 m/s ² peak acceleration at 1000 Hz
VPD Syringe Outlet Diameter	861 μm
GPD Delivery Tube Size	1 mm
GPD Delivery Tube Incline	50°
GPD Tube Offset from Surface	4.0 mm
Gas Flow Coaxial with Laser	2 l/min argon
Gas Flow Perpendicular to Laser	2 l/min argon
Laser Power	1250 W
Process Feed Rate	1000 mm/min

The results from five trials are listed below in Table 18, and pictures of some of the printed tracks can be seen in Figure 35. The average powder capture efficiency using vibratory powder feeding is 94.9% with a range of 8.6%, demonstrating that the system is very capable of high capture efficiency and that there is room for improvement on a system level. This level of powder capture meets the research goal of 95%.

Table 18: Experimental Powder Capture Efficiency Results

Trial Number	Mass Flow Rate [g/min]	Powder Capture Efficiency [%]
1	7.80	98.1
2	7.78	96.0
3	7.72	89.5
4	7.45	98.0
5	7.48	93.1

To offer a fair comparison, the same powder capture efficiency test was run using the conventional system with conditions matched as close as possible to the previous experiment, including no shielding gas flow. The test conditions are outlined in

Table 19 and photographs of the results are shown in Figure 35. The average measured powder capture efficiency was 73.1% with a range of 3.4% at a calibrated mass flow rate of 8.14 g/min.

Table 19: Conventional System Powder Capture Efficiency Test Settings

Parameter	Value
Laser Power	1250 W
Process Feed Rate	1000 mm/min
Standoff	10 mm
Powder Gas Flow Rate	3 l/min
Laser Coaxial Gas Flow Rate	2 l/min
Shield Gas Flow Rate	0 l/min

When the tracks printed by both systems are compared, they are largely similar with the following differences:

- The conventional process has significantly less surface oxidation. This is expected as little work was done to optimize the gas flows in the experimental system which could prevent the hot track from contacting oxygen in the atmosphere.
- The track width is more consistent for the conventional process, and it is unknown if the small variations in the experimental tracks are because of the oxide formation caused by poor shielding, variations in the powder flow, or other factors.
- The experimental track shape varied slightly with process direction (in Figure 35, the top track of each part was printed right-to-left and the bottom left-to-right). This is most likely a result of small imperfections in the system parts causing some misalignment between the powder stream, gas streams, and laser beam.
- The surface roughness of the experimental system's tracks is significantly lower, which is expected from a system with higher powder capture efficiency. A low capture efficiency process has particles landing outside of the melt pool where they can fuse but not completely melt and integrate into the part.

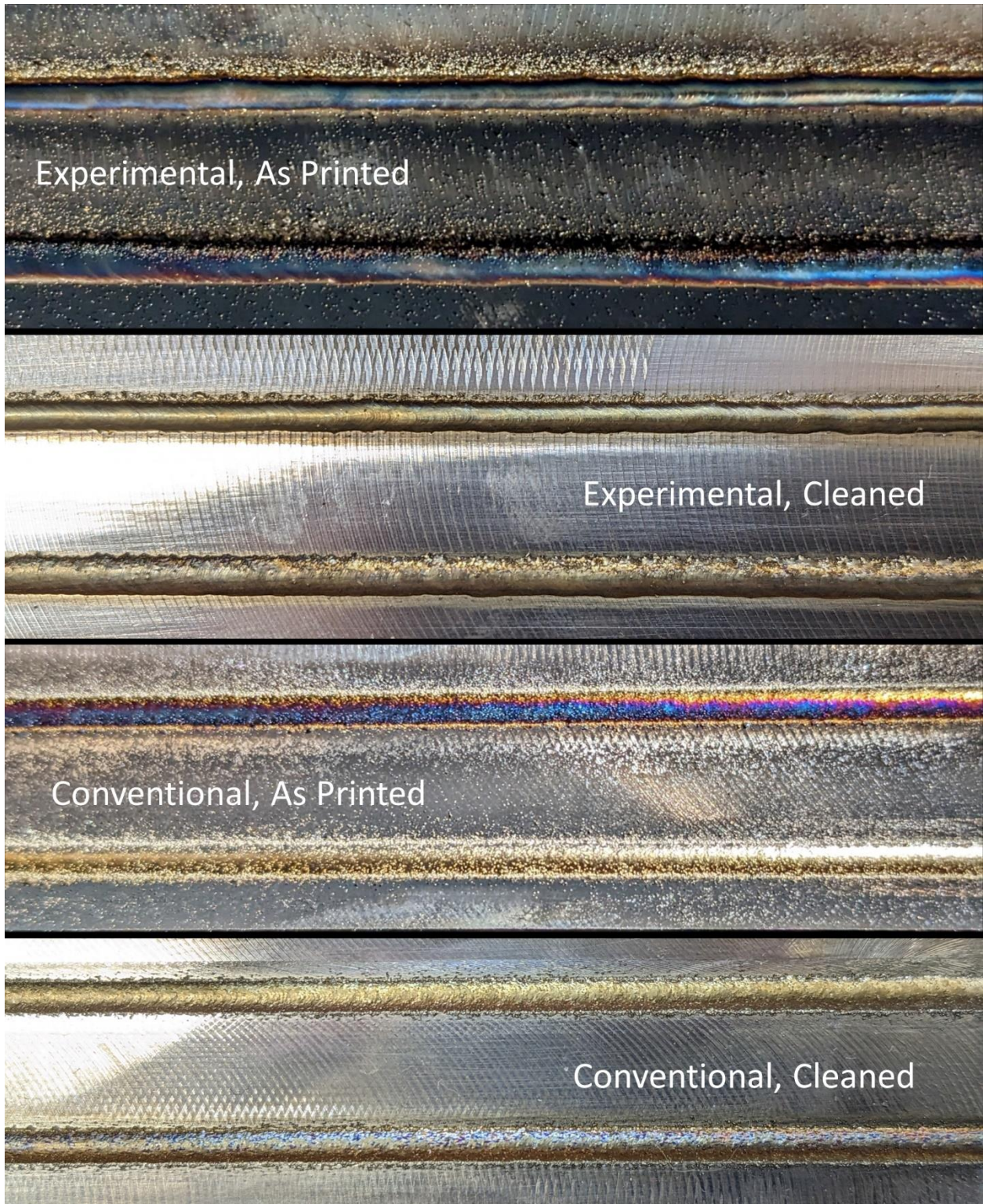


Figure 35: Comparison of Printed Tracks from Experimental and Conventional Systems in As Printed and Cleaned Conditions

9. Conclusions

At the conclusion of this work, the six goals set forth as part of the three stated research questions have been met successfully. The approach of using a tapered dispensing tip with a capillary tube end and incline control proved to give good results in vibration powder dispensing. Usable flow rates with low in-run variability and monotonic control were all achieved. The following conclusions about vibration powder dispensing are strictly speaking only applicable to the stainless steel powder and dispensing tips used in this study:

- Incline has a positive monotonic relationship with dispensed mass flow rate.
- Dispensing tip diameter also has a positive monotonic relationship with dispensed mass flow rate but is not suitable for continuous control.
- Vibration frequency and acceleration offered little control of the dispensed mass flow rate.
- The variability of dispensed mass flow rate within one run is very low and comparable to the conventional delivery system.
- The variability of dispensed mass flow rate between runs is relatively high, likely due to powder loading. This is an important area of investigation for the continuation of this work.

Performing gravity-fed powder delivery with an inclined tube also proved successful in meeting the goals set forth in this work. The following conclusions should only be applied to the specific conditions studied, but not with the same strictness as vibration powder dispensing:

- Power stream spread was affected primarily by tube diameter and secondarily by the mass flow rate. Tube length and incline did not have significant effects.
- Powder stream velocity was affected by tube incline primarily and tube diameter secondarily. Tube length and mass flow rate did not have significant effects in the ranges studied.
- Simulation results showed that coefficient of static friction and coefficient of restitution of the tube have a significant effect on the behavior of the spread and velocity.

Understanding the vibration powder dispensing and gravity-fed powder delivery systems allowed power capture efficiency experiments with excellent outcomes. High powder capture efficiency of 94.9% was achieved compared with 73.1% using the conventional system. The experimental system also achieved a visually lower surface roughness in the deposited bead than the conventional system. The experimental system had a usable but imperfect shielding gas system which allowed the system to operate but left an undesirable amount of surface oxidation. This is an important area of investigation for the continuation of this work.

The combination of high powder capture efficiency, fast on and off times for powder delivery, and a small minimum mass loading requirement make this type of system well-suited for not only reducing operating costs of standard DED processes, but also enabling processes in which it is desirable to use a very small load of powder, such as a screening

experiment in materials development or to make a small part out of an expensive material. Additionally, the fast response time can enable multi-material printing with more abrupt composition changes than a conventional system.

9.1. Extensions and Future Work

In the context of engineering a system to dispense and deliver powder to a DED process, this work serves as a proof of concept, expanding on and replicating the work done by Wang and Li [2]. Both sets of work demonstrate the viability of vibration powder feeding and gravity-fed powder dispensing for a limited set of powders in a few system configurations. The next appropriate step would be concept development and planning, with the most important output being a basic mapping of system configuration and powder properties to performance. Knowing how powder of a given material with a certain size, shape and surface properties will perform with certain system parameters (diameters, inclines, vibration settings, materials, etc.) is crucial to creating a broadly applicable design. The methods used in this work can be used as a basis for characterizing powder and system behavior, and there is room for improving the speed and accuracy of the methods. Other system designs like the annular arrangement used by Wang and Li [2] should also be assessed as part of concept selection. If viable concepts are found, work can then continue into detailed design and other development stages.

Application areas for vibration powder dispensing exist outside of DED, some of which may benefit from the mass flow rate control offered by using inclined dispensing systems. Other authors have noted the following application areas for vibration powder dispensing:

- Creating multi-material features in other additive manufacturing processes, most often powder-bed based ones [12, 14]
- Pharmaceutical dosing and production [12, 31]
- Composite materials made from powders [13]
- High throughput combinatorial experiments in metallurgy [32] and other fields

10. References

- [1] ASTM, 2012, "Standard Terminology for Additive Manufacturing Technologies."
- [2] Wang, W., and Li, L., 2011, "High-Quality High-Material-Usage Multiple-Layer Laser Deposition of Nickel Alloys Using Sonic or Ultrasonic Vibration Powder Feeding," Proceedings of the Institution of Mechanical Engineers, Part B: Journal of Engineering Manufacture, 225(1), pp. 130-139.
- [3] Katinas, C., Shang, W., Shin, Y. C., and Chen, J., 2018, "Modeling Particle Spray and Capture Efficiency for Direct Laser Deposition Using a Four Nozzle Powder Injection System," Journal of Manufacturing Science and Engineering, 140.
- [4] Unocic, R. R., and DuPont, J. N., 2004, "Process Efficiency Measurements in the Laser Engineered Net Shaping Process," Metallurgical and Materials Transactions B, 35B(1), pp. 143-152.
- [5] Wang, F., Mei, J., and Wu, X., 2006, "Microstructure study of direct laser fabricated Ti alloys using powder and wire," Applied Surface Science, 253(3), pp. 1424-1430.
- [6] Sandia National Labs, 1997, "News Release - Laser Engineered Net Shaping (LENS)," <https://www.sandia.gov/media/lens.htm>.
- [7] MarketReserach.biz, 2018, "Metal 3D Printer Market By Type (Powder Bed, Powder Directed Energy Deposition, Wire Directed Energy Deposition) By Application (Medical, Aerospace & Defense, Automotive, Fashion & Aesthetics) And Region - Global Forecast 2026," <https://marketresearch.biz/report/metal-3d-printer-market/#details>.
- [8] Yang, S., and Evans, J. R. G., 2003, "Computer control of powder flow for solid freeforming by acoustic modulation," Powder Technology, 133(1-3), pp. 251-254.
- [9] Yang, S., and Evans, J. R. G., 2004, "A multi-component powder dispensing system for three dimensional functional gradients," Materials Science and Engineering: A, 379(1-2), pp. 351-359.
- [10] Chen, X., Seyfang, K., and Steckel, H., 2012, "Development of a micro dosing system for fine powder using a vibrating capillary. Part 1: the investigation of factors influencing on the dosing performance," Int J Pharm, 433(1-2), pp. 34-41.
- [11] Lu, X., Yang, S., and Evans, J. R., 2009, "Microfeeding with different ultrasonic nozzle designs," Ultrasonics, 49(6-7), pp. 514-521.
- [12] Lu, X., Yang, S., and Evans, J. R. G., 2007, "Dose uniformity of fine powders in ultrasonic microfeeding," Powder Technology, 175(2), pp. 63-72.
- [13] Matsusaka, S., Yamamoto, K., and Masuda, H., 1996, "Micro-feeding of a Fine Powder Using a Vibrating Capillary Tube," Advanced Powder Technology, 7(2), pp. 141-151.
- [14] Kumar, P., Santosa, J. K., Beck, E., and Das, S., 2004, "Direct-write Deposition of Fine Powders Through Miniature Hopper-Nozzles for Multi-material Solid Freeform Fabrication," Rapid Prototyping Journal, 10(1), pp. 14-23.
- [15] Jiang, Y., Matsusaka, S., Masuda, H., and Qian, Y., 2009, "Development of measurement system for powder flowability based on vibrating capillary method," Powder Technology, 188(3), pp. 242-247.
- [16] Ishii, K., Suzuki, M., Segawa, T., Kihara, Y., Yasuda, M., and Matsusaka, S., 2011, "Flowability measurement of pulverized and granulated materials using vibrating tube method," Advanced Powder Technology, 22(3), pp. 319-323.

- [17] Yang, S., and Evans, J. R. G., 2005, "On the rate of descent of powder in a vibrating tube," *Philosophical Magazine*, 85(10), pp. 1089-1109.
- [18] "EDEM," Altair.
- [19] DEM Solutions Ltd., 2016, "What is DEM."
- [20] Li, Y., Xu, Y., and Thornton, C., 2005, "A comparison of discrete element simulations and experiments for 'sandpiles' composed of spherical particles," *Powder Technology*, 160(3), pp. 219-228.
- [21] "MATLAB," MathWorks.
- [22] Morrissey, J. P., Thakur, S. C., and Ooi, J. Y., 2014, "EDEM Contact Model: Adhesive Elasto-Plastic Model," School of Engineering, University of Edinburgh.
- [23] MatWeb, 2022, "AK Steel 316L Austenitic Stainless Steel," <https://www.matweb.com/search/DataSheet.aspx?MatGUID=9e9ab696974044cab4a7fd83687934eb>.
- [24] Li, X., Dunn, P. F., and Brach, R. M., 1999, "Experimental and Numerical Studies on the Normal Impact of Microspheres with Surfaces," *Journal of Aerosol Science*, 30(4), pp. 439-449.
- [25] DEM Solutions Ltd., 2019, "Calibrating DEM Models for Powder Simulation."
- [26] Cole, S., 2015, "Particle Shear Modulus-It Can Save You Time."
- [27] Meier, C., Weissbach, R., Weinberg, J., Wall, W. A., and Harta, A. J., 2019, "Modeling and Characterization of Cohesion in Fine Metal Powders with a Focus on Additive Manufacturing Process Simulations," *Powder Technology*, 343(1), pp. 855-866.
- [28] ASTM, 2017, "Standard Test Method for Apparent Density of Free-Flowing Metal Powders Using the Hall Flowmeter Funnel."
- [29] ASTM, 2015, "Standard Test Method for Tap Density of Metal Powders and Compounds."
- [30] ASTM, 2017, "Standard Test Method for Flow Rate of Metal Powders Using the Hall Flowmeter Funnel."
- [31] Wang, H., Wu, L., Zhang, T., Chen, R., and Zhang, L., 2018, "Continuous micro-feeding of fine cohesive powders actuated by pulse inertia force and acoustic radiation force in ultrasonic standing wave field," *Int J Pharm*, 545(1-2), pp. 153-162.
- [32] Yang, S., and Evans, J. R., 2004, "Device for Preparing Combinatorial Libraries in Powder Metallurgy," *Journal of Combinatorial Chemistry*, 6, pp. 549-555.